

See discussions, stats, and author profiles for this publication at: <https://www.researchgate.net/publication/311320041>

Numerical investigation of a viscous regularization of the Euler equations by Entropy Viscosity

Article in *Computer Methods in Applied Mechanics and Engineering* · April 2017

DOI: 10.1016/j.cma.2016.12.010

CITATIONS

13

READS

1,247

2 authors:



[Murtazo Nazarov](#)

Uppsala University

35 PUBLICATIONS 411 CITATIONS

[SEE PROFILE](#)



[Aurélien Larcher](#)

MINES ParisTech

25 PUBLICATIONS 165 CITATIONS

[SEE PROFILE](#)

Some of the authors of this publication are also working on these related projects:



Nonlinear stabilization methods [View project](#)



FEniCS-HPC [View project](#)

Numerical investigation of a viscous regularization of the Euler equations by Entropy Viscosity

Murtazo Nazarov^{a,*}, Aurélien Larcher^b

^a*Division of Scientific Computing, Department of Information Technology, Uppsala University, Sweden*

^b*ERCIM ABCDE Fellow, Department of Mathematical Sciences, NTNU, Trondheim, Norway*

Abstract

The Navier–Stokes viscous fluxes are a well-known viscous regularization of the Euler equations. However, since these fluxes do not add any viscosity to the mass equation, the positivity of density is violated. This paper investigates a new class of viscous regularization of the Euler equations, which was recently proposed by Guermond & Popov [SIAM J. Appl. Math., 74-2 (2014) pp. 284-305]. In contrast to the Navier–Stokes fluxes, the new regularization adds a viscous term to the mass equation. Since non-physical viscous terms are used, it is important to show that the exact solution’s properties, such as the location of shocks, contact and rarefaction waves are not violated. The present study concerns a careful numerical investigation of the new viscous regularization in a number of well-known 1D and 2D benchmark problems. Also, a direct numerical comparison with respect to the physical Navier–Stokes regularization is shown. The numerical tests show that the entropy viscosity method can achieve high order accuracy for any polynomial degrees. Detailed algorithms for the implementation of a slip wall boundary condition are presented in a weak and strong form.

Keywords: Entropy viscosity, parabolic regularization, conservation laws, compressible flow, Euler equations, finite elements, nonlinear stabilization

1. Introduction

One of the big challenges in Computational Fluid Dynamics is to design and implement efficient high-order accurate numerical methods for approximating nonlinear hyperbolic systems of conservation laws. Since high order discretizations produce spurious oscillations in shock regions, nonlinear stabilization techniques are needed to avoid or control these oscillations. There exists a large class of methods addressing the question of instabilities of high-order methods and most of them rely on flux/slope limiters. The design of limiters is not an easy task, especially in the case of unstructured meshes. One of the traditional ways of solving the entropy solution of conservation laws consists in adding an artificial viscosity term: a mesh dependent parabolic operator. This approach has been introduced by Von Neumann and Richtmyer in 50s for the numerical approximation of conservation laws. The classical artificial viscosity term is constructed to be proportional to the gradient of the solution, which loses regularity near shock and sharp discontinuities. To overcome this issue, a residual based stabilization term is used in Astreamline Upwind Petrov–Galerkin schemes (SUPG) by Hughes and Mallet [1]. Later, Johnson et al. added an isotropic residual based artificial viscosity to SUPG [2] to obtain the convergence to the unique entropy solution. Recently, it has been shown in [3] that Streamline Diffusion terms are not necessary for the method to converge. The nonlinear isotropic viscosity is the main ingredient for the L^∞ -bound and the convergence. Dropping Streamline Diffusion terms, simplifies the scheme significantly and there will be no demand to keep the method implicit, see e.g., [4] and [5] where the residual based artificial viscosity method is successfully applied for systems of compressible Euler equations using explicit Runge–Kutta methods.

*Corresponding author

Email address: murtazo.nazarov@it.uu.se (Murtazo Nazarov)

In practice the nonlinear artificial viscosity is constructed locally in each cell, which may introduce nonphysical oscillations in the solution. The work by Barter and Darmofal [6] and Reisner et al. [7] constructs a smoother variation of artificial viscosity by solving additional scalar reaction-diffusion equation. This approach removes small nonphysical oscillations introduced by non-smooth viscosity and does not pollute the solution in the downstream region.

The so-called *entropy viscosity* method was first introduced by Guermond et al. [8, 9], where the diffusive coefficient is constructed using the entropy residual. The key feature of the entropy viscosity method is that the amount of artificial viscosity it introduces, is determined by the size of the entropy residual. Scalar conservation equations have infinitely many entropy pairs and all physical systems have at least one entropy function satisfying an auxiliary entropy equation/inequality. The entropy “equation” is an equation only in the regions where the solution is smooth and it becomes an inequality in the shock regions. This inequality acts as a selection principle for choosing the physically relevant solution. The amount of violation of the entropy equation is called entropy production or entropy residual. The main idea is that there is a large entropy production in strong shocks (it can be proved in simple cases that the entropy production is a Dirac measure supported in shocks) which then activates the entropy viscosity wherever a shock or a discontinuity is traced. In this paper, the entropy viscosity is constructed on the finite element nodes rather than on the cells. This definition of the viscosity turns out to be more accurate especially for higher polynomial spaces.

Physics-based viscous fluxes or Navier–Stokes viscous terms are widely used in the literature in numerical approximations of compressible Euler equations. For instance, we refer to [10, 6, 11] for discontinuous Galerkin, [9, 12, 13, 4] for continuous Galerkin and [14, 5] for spectral element methods, where the artificial viscosity terms are constructed via physics based viscosity. In above-mentioned references, several high-order numerical algorithms for the construction of artificial viscosity coefficient are proposed and many realistic flow problems in different physics are solved.

However, since the Navier–Stokes fluxes do not involve any viscosity in the mass equation, the solution suffers from the so-called Gibbs phenomenon and introduces dissipation errors when using non-smooth initial data: or, more precisely, the so-called positivity property of density cannot be guaranteed. By constructing very simple flow scenarios one can show that Navier–Stokes fluxes violate the positivity properties of the density and internal energy, and do not satisfy entropy inequalities, see [15, Sec 2.4.]. These theoretical findings question the usage of the Navier–Stokes fluxes to regularize the Euler equations. Recently, a general class of viscous regularization of the Euler equations, that satisfy all above-mentioned thermodynamic properties, was introduced by Guermond and Popov [15], which is coined as Guermond–Popov fluxes in this paper.

In [16], the Guermond–Popov fluxes are used to solve compressible flow in various speeds for linear finite element approximation. The main goal of this paper is to investigate the Guermond–Popov fluxes numerically in continuous finite element setting in arbitrary polynomial degrees and space dimensions. Since, this is an alternative to the standard physics based viscous terms, it is important to show at least numerically that the method converges to the entropy solution. For instance, computing correctly the position of shocks, contact discontinuities and rarefaction waves are one of the main requirements that need to be assessed.

Most applications involving the compressible Euler system require to impose the so-called slip boundary condition, i.e., normal velocity should vanish on the boundary. This boundary condition is challenging to implement for general complex geometries. In this paper two different approaches to impose this boundary condition are discussed, namely weakly and strongly, for compressible flows and compare their performance using a realistic flow problem. The strong implementation of slip boundary condition for incompressible flow was reported earlier in [17] and [18].

The problem formulation is stated in Section 2. Next, Section 3 recalls the standard Navier–Stokes fluxes and introduces the Guermond–Popov regularization, together with the finite element space discretization and the time approximation. Further details of the implementations of weak and strong slip boundary conditions are provided in Section 4. Finally, the performance of the method is illustrated in Section 5 with various benchmark problems.

2. The basic equations

Let us consider a fluid enclosed in a fixed (open) domain Ω in \mathbb{R}^d , $d = 1, 2, 3$, with boundary Γ over a time interval $[0, \hat{t}]$, where \hat{t} is the final time.

The *density* ρ , *momentum* $\mathbf{m} = \rho \mathbf{u}$, with $\mathbf{u} = (u_1, \dots, u_d)$ the *velocity*, and the *total energy* E as functions of $(\mathbf{x}, t) \in Q = \Omega \times [0, \hat{t}]$, where $\mathbf{x} = (x_1, \dots, x_d)$ denotes the coordinates in \mathbb{R}^d , are solution to the Euler equations in

conservative form:

$$\partial_t \mathbf{U} + \nabla \cdot \mathbf{F}(\mathbf{U}) = \mathbf{0}, \quad \mathbf{U} = \begin{pmatrix} \rho \\ \mathbf{m} \\ E \end{pmatrix}, \quad \mathbf{F}(\mathbf{U}) = \begin{pmatrix} \mathbf{m} \\ \mathbf{m} \otimes \mathbf{u} + p \mathbb{I} \\ \mathbf{u}(E + p) \end{pmatrix}, \quad (1)$$

where $p = p(\mathbf{x}, t)$ is the *pressure* of the fluid, \otimes denotes the tensor product, \mathbb{I} denotes the identity matrix in \mathbb{R}^d , $\mathbf{u} := \mathbf{m}/\rho$ is the velocity field, $\partial_t = \partial/\partial t$ and $\mathbf{0}$ is the zero vector. The Euler equations are supplemented with the initial condition $\mathbf{U}(\mathbf{x}, 0) = \mathbf{U}_0(\mathbf{x})$, where $\mathbf{U}_0(\mathbf{x})$.

Furthermore, the total energy is defined as $E = \mathfrak{K} + \rho e$, where $\mathfrak{K} = \rho |\mathbf{u}|^2/2$ is the *kinetic energy*, with $|\mathbf{u}|^2 \equiv u_1^2 + \dots + u_d^2$, and e is the *internal energy*.

As the number of unknowns including the pressure is $d + 3$ but there are only $d + 2$ equations in (1), the Euler system is supplemented with a closure equation, namely the *equation of state* of an *ideal gas*:

$$p = \rho T = (\gamma - 1)(E - \rho |\mathbf{u}|^2/2), \quad (2)$$

expressing the pressure p as a function of density ρ and *temperature* T . Here γ is the *adiabatic gas constant*. The Euler system is known to have a physical *entropy functional*

$$S(p, \rho) = \frac{\rho}{\gamma - 1} \log \frac{p}{\rho^\gamma},$$

which satisfies the following entropy inequality, see e.g., [19]

$$\partial_t S + \nabla \cdot (\mathbf{u} S) \geq 0, \quad (3)$$

which holds as an equality if all fields are smooth. Moreover, the so-called *specific entropy* is a functional derived from the density and internal energy, denoted as $s(e, \rho)$.

For a perfect gas, the *speed of sound* c is given by $c^2 = \gamma p/\rho$, and the *Mach number* is defined as $M = |\mathbf{u}|/c$, with \mathbf{u} the velocity of the gas.

3. Viscous regularization of the Euler system

It is well-known that the Galerkin approximation by finite elements of (1) is not stable. Mesh-dependent viscous fluxes are usually added to the discrete approximation of the system to circumvent this stability issue:

$$\partial_t \mathbf{U} + \nabla \cdot \mathbf{F}(\mathbf{U}) - \nabla \cdot \mathbf{F}_{\text{visc}}(\mathbf{U}) = \mathbf{0}, \quad (4)$$

where \mathbf{F}_{visc} is a viscous flux which will be considered throughout this paper under two forms: a traditional Navier–Stokes viscous flux, and a new class of regularization terms which is referred to as Guermond–Popov flux.

3.1. Navier–Stokes viscous fluxes

The compressible Navier–Stokes equations are obtained by adding the following viscous fluxes to (1)

$$\mathbf{F}_{\text{NS-visc}}(\mathbf{U}) = \begin{pmatrix} 0 \\ 2\mu \nabla^s \mathbf{u} + \lambda \nabla \cdot \mathbf{u} \mathbb{I} \\ \kappa \nabla T + (2\mu \nabla^s \mathbf{u} + \lambda \nabla \cdot \mathbf{u} \mathbb{I}) \cdot \mathbf{u} \end{pmatrix}, \quad (5)$$

where $\kappa \geq 0$ is the thermal conduction, $\nabla^s \mathbf{u} = \frac{1}{2}(\nabla \mathbf{u} + \nabla \mathbf{u}^T)$, $\mu > 0$ and $\lambda + 2\mu > 0$ are viscosity parameters. The Euler equations are recovered at the limit when these viscosity parameters tend to zero.

The Navier–Stokes fluxes stand as a common technique for the numerical computations of the Euler equations, see for example [9, 12, 4]. However, it was proven in [20] and it was recently mentioned in [15] that, when the thermal diffusivity κ is non-zero, the usual Navier–Stokes regularization violates the minimum entropy principle and, moreover, the resulting system does not admit any generalized entropy inequalities.

For example, let us consider the case where the Navier–Stokes regularization is used to solve a contact line problem starting at $x_1 = 0$, i.e. $\rho = \rho_l$ if $x_1 < 0$, and $\rho = \rho_r$ if $x_1 \geq 0$, $\rho_l > \rho_r$; $\mathbf{u} = \mathbf{u}_0$, $p = p_0$, where \mathbf{u}_0 and p_0 are given constants. Under these assumptions, the mass equation is equivalent to an advection equation with moving discontinuous profile of the density with a constant speed \mathbf{u}_0 : $\partial_t \rho + \nabla \cdot (\mathbf{u}_0 \rho) = 0$, and by taking into account the mass conservation, the energy equation transforms into

$$\partial_t(e\rho) + \nabla \cdot (\mathbf{u}_0 e\rho) - \nabla \cdot (\kappa \nabla T) = 0. \quad (6)$$

For a polytropic ideal gas the equation of state (2) implies that $p_0 = \rho T = (\gamma - 1)\rho e$, i.e., the last equation is true only for $\kappa = 0$. In other words, the above discussion justifies that the Navier–Stokes regularization is not compatible with contact waves.

It should be noted that solving the contact line problem numerically when $\kappa = 0$ is difficult since the solution oscillates due to the Gibbs phenomenon: more precisely, both the positivity of the density and the internal energy are violated.

3.2. New class of regularization of the Euler equations

Let us now consider the Guermond–Popov fluxes [15] to regularize the compressible Euler equations (1)

$$\mathbf{F}_{\text{GP-visc}}(\mathbf{U}) = \begin{pmatrix} f \\ \mu \rho \nabla^s \mathbf{u} + f \otimes \mathbf{u} \\ \kappa \nabla(\rho e) + \frac{\mathbf{u}^2}{2} f + \mu \rho \nabla^s \mathbf{u} \cdot \mathbf{u} \end{pmatrix}, \quad (7)$$

where $f := \kappa \nabla \rho$, and $\kappa > 0$ and $\mu > 0$ are viscosity coefficients.

The objective of this class of regularization is to obtain the invariant domain property for the density and internal energy, a minimum principle on the specific entropy, and compatibility for large class of entropy inequalities. The following two important results are obtained in [15].

Theorem 1. *Any weak solution of the regularized system by Guermond–Popov fluxes satisfy the entropy inequality*

$$\partial_t(\rho g(s)) + \nabla \cdot (\mathbf{u} \rho g(s)) + \nabla \cdot (\mathbf{u} \rho g(s) - \kappa \nabla(\rho g(s))) \geq 0,$$

for all generalized Harten’s entropies $\rho g(s)$, see [21, 19], where $g \in C^2$, $g' \frac{\gamma}{\gamma-1} > g''$, $g' > 0$.

Proof. See [15, Theorem 4.1]. □

Theorem 2. *Assume that solution to the regularized system is smooth. Then the solution of (4) using regularization (7) satisfies*

(i) *positivity of density:*

$$\text{ess inf}_{\mathbf{x} \in \mathbb{R}^d} \rho(\mathbf{x}, t) \geq 0, \quad \forall t > 0.$$

(ii) *minimum principle for specific entropy:*

$$\inf_{\mathbf{x} \in \mathbb{R}^d} s(\mathbf{x}, t) \geq \inf_{\mathbf{x} \in \mathbb{R}^d} s(\mathbf{x}, 0), \quad \forall t > 0.$$

Proof. See [15, Lemma 3.1, 3.2 and Theorem 3.5]. □

As an example let us consider the contact line problem discussed in Section 3.1, i.e., the density has a discontinuity whereas velocity and pressure are constant functions. Let $\rho(\mathbf{x}, 0) = \rho_0(\mathbf{x})$ be an initial density. Consequently, if $\mathbf{u}(\mathbf{x}, t) = \mathbf{u}_0$, $p(\mathbf{x}, t) = p_0$ and $\rho(\mathbf{x}, t)$ solves the mass equation

$$\partial_t \rho + \nabla \cdot (\mathbf{u}_0 \rho) - \nabla \cdot (\kappa \nabla \rho) = 0, \quad (8)$$

which should also solve the momentum and energy equations. In fact, when the velocity and pressure are constant the momentum equation easily simplifies into (8). By virtue of (8) the energy equation simplifies to

$$\partial_t(e\rho) + \nabla \cdot (\mathbf{u}_0 e\rho) - \nabla \cdot (\kappa \nabla(e\rho)) = 0. \quad (9)$$

Equation (9) holds for a polytropic ideal gas with the above equation of states $p_0 = \rho T = (\gamma - 1)\rho e$: this example shows that the Guermond–Popov fluxes are compatible with contact waves.

For further discussions and detailed mathematical analysis of the Guermond–Popov regularization, the reader is referred to [15].

3.3. Entropy Viscosity

To make the regularization higher order in space, viscosity coefficients are constructed using the so-called *entropy viscosity* method, a nonlinear stabilization technique that was first introduced in [8, 9]. By making the numerical diffusion proportional to the entropy production, the entropy viscosity technique adds a large numerical dissipation in the shock regions and sharp discontinuities, while almost no dissipation is enforced in regions where the solution remains smooth. This simple idea is mesh- and approximation- independent and has already been shown to be efficient in [8, 9, 22, 23, 11, 16].

3.4. Finite element approximation

Let \mathcal{T}_h be a mesh defined as a subdivision of Ω into disjoint elements K such that $\overline{\Omega} = \cup_{K \in \mathcal{T}_h} \overline{K}$; $\overline{\Omega}$ and \overline{K} are the closure of Ω and K , respectively. The mesh is assumed to be affine to avoid unnecessary technicalities, i.e., Ω is a polygon in two space dimensions or a polyhedron in three space dimensions. For each cell K in the mesh let us denote $\mathbf{g}_K : \widehat{K} \rightarrow K$ the affine mapping that maps the reference element \widehat{K} to K . Let us consider a family of meshes $\{\mathcal{T}_h\}_{h>0}$ such that this family is shape-regular and each mesh is conforming.

For each mesh \mathcal{T}_h , a continuous approximation space is defined as follows:

$$\mathcal{X}_h = \{v_h \in C^0(\overline{\Omega}); \forall K \in \mathcal{T}_h, v_h|_K \circ \mathbf{g}_K \in \mathbb{P}_k\}, \quad (10)$$

where \mathbb{P}_k is the set of multivariate polynomials of total degree at most $k \geq 1$ defined over \widehat{K} . Throughout this paper, Lagrange finite elements are considered, with N_1, \dots, N_I the collection of all the Lagrange nodes in the mesh \mathcal{T}_h and $\{\varphi_1, \dots, \varphi_I\}$ the associated scalar-valued shape functions.

All the scalar-valued independent variables and the Cartesian components of the momentum are approximated in \mathcal{X}_h , i.e., $\rho_h, E_h \in \mathcal{X}_h$, $\mathbf{m}_h \in \mathcal{X}_h^d =: \mathcal{X}_h$. Let us define \mathbf{u}_h , p_h and T_h to be finite element functions in \mathcal{X}_h , \mathcal{X}_h and \mathcal{X}_h , respectively, which are defined by their nodal values given by

$$\begin{aligned} \mathbf{u}_h(N_i, t) &= \mathbf{m}_h(N_i, t) / \rho_h(N_i, t), \\ p_h(N_i, t) &= \rho_h(N_i, t) T_h(N_i, t), \\ T_h(N_i, t) &= (\gamma - 1) \left(E_h(N_i, t) / \rho_h(N_i, t) - \frac{1}{2} |\mathbf{u}_h(N_i, t)|^2 \right) \end{aligned} \quad (11)$$

for all nodes N_1, \dots, N_I in the mesh \mathcal{T}_h . For the sake of clarity the following simplified notation is introduced

$$\mathbf{U}_h := (\rho_h, \mathbf{m}_h, E_h)^T \in \mathcal{W}_h := \mathcal{X}_h \times \mathcal{X}_h \times \mathcal{X}_h. \quad (12)$$

Therefore the finite element approximation of the compressible Euler equations (1) reads: find $\mathbf{U}_h(t) \in C^1([0, \hat{t}]; \mathcal{W}_h)$, such that

$$(\partial_t \mathbf{U}_h, \mathbf{V}_h) + (\nabla \cdot \mathbf{F}(\mathbf{U}_h), \mathbf{V}_h) + (\mathbf{F}_{\text{visc}}(\mathbf{U}_h), \nabla \mathbf{V}_h) - (\mathbf{n} \cdot \mathbf{F}_{\text{visc}}(\mathbf{U}_h), \mathbf{V}_h)_\Gamma = \mathbf{0}, \quad (13)$$

for all test functions $\mathbf{V}_h \in \mathcal{W}_h$, where $(\mathbf{v}, \mathbf{w}) = \sum_{K \in \mathcal{T}_h} \int_K \mathbf{v} \cdot \mathbf{w} \, d\mathbf{x}$, $(\mathbf{v}, \mathbf{w})_{\partial\Omega} = \sum_{K \in \mathcal{T}_h} \int_{\partial K \setminus \partial\Omega} \mathbf{v} \cdot \mathbf{w} \, d\mathbf{s}$, \mathbf{n} is unit outward normal to ∂K , and the viscous fluxes $\mathbf{F}_{\text{visc}}(\mathbf{U}_h)$ is the viscous stabilization which is either standard Navier–Stokes or Guermond–Popov fluxes. In practice, in the FEniCS project [24, Chapter 11] which is used to perform the numerical computations of this paper, all numerical integration are computed exactly by automatically determining the quadrature degree with respect to the polynomial space and the complexity of the underlying integrand.

At each time step, the residual of the entropy equation is evaluated to compute the associated artificial viscosities, and then the system is solved to update mass, momentum, and total energy.

Let us denote the entropy residual by $R_h \in C^1([0, \hat{t}]; \mathcal{X}_h)$ and corresponding interface contribution by $J_h \in C^1([0, \hat{t}]; \mathcal{X}_h)$. Then for all nodes N_1, \dots, N_I in the mesh \mathcal{T}_h we propose to compute the nodal values of R_h and J_h using the following integrals:

$$R_h(N_i, t) := \sum_{K \in \mathcal{T}_h} \frac{1}{|K|} \int_K |\partial_t S_h + \nabla \cdot (\mathbf{u}_h S_h)| \varphi_i \, d\mathbf{x}, \quad (14)$$

$$J_h(N_i, t) := \sum_{F \in \mathcal{F}_h} \frac{1}{|F|} \int_F |\mathbf{u}_h \cdot \mathbf{n} \llbracket \partial_n S_h \rrbracket| \varphi_i \, ds, \quad (15)$$

where F denotes a face of K and assume that it is an interface, i.e., F is not a boundary face, \mathcal{F}_h denotes the set of the interfaces in the mesh, $|K|$ and $|F|$ denote the measure of K and F respectively, and $\llbracket q \rrbracket$ denotes the jump of q across facet F .

Furthermore, the discrete mesh-size function $h(\mathbf{x})$ is constructed as the following continuous piece-wise linear function: for every nodal point N_i ,

$$h(N_i) := \min(h_K/k, \forall K \in \mathcal{T}_h \text{ such that } N_i \in K),$$

where h_K is the smallest edge of K .

Finally, a nodal entropy viscosity is defined for each nodal point N_i of the mesh \mathcal{T}_h , as the kinematic viscosity computed as follows:

$$\mu_{\text{ent}}(N_i, t) := h(N_i)^2 \frac{\max(|R_h(N_i, t)|, |J_h(N_i, t)|)}{\|S_h(N_i, t) - \overline{S_h(N_i, t)}\|_{L^\infty(\Omega)}}, \quad (16)$$

where $\overline{S_h} = \frac{1}{|\Omega|} \int_\Omega S_h$, and the residual and the jump are normalized with the L^∞ -norm of the entropy functional minus its average in the whole domain. Note that the entropy residual detects the shock region, while the jump term is active in other discontinuities such as contact waves. This definition of entropy viscosity is more dissipative than the original algorithm proposed in [8] and [9], therefore is more robust. The usage of the jump term in the definition of the entropy viscosity was first used in [25] to construct a similar viscosity (they take the sum of the interior residual and the jump term).

The maximum kinematic viscosity over each nodes, μ_{\max} , is evaluated as follows:

$$\mu_{\max}(N_i, t) = c_{\max} h(N_i) \left(|\mathbf{u}_h(N_i, t)| + \sqrt{\gamma T_h(N_i, t)} \right). \quad (17)$$

Finally viscosities are defined as:

$$\mu_h(N_i, t) = \min(\mu_{\max}(N_i, t), c_{\text{ent}} \mu_{\text{ent}}(N_i, t)), \quad (18)$$

$$\kappa_h(N_i, t) = \min(\mu_{\max}(N_i, t), \mathcal{P} \mu_{\text{ent}}(N_i, t)), \quad (19)$$

where \mathcal{P} is an artificial Prandtl number, c_{\max} and c_{ent} are user defined control parameters. In the presented computations, the parameter values were $\mathcal{P} = 0.4$, 1 , $c_{\max} = 0.25$ and $c_{\text{ent}} = 1$.

Note that the above definition of the entropy viscosity is a nodal based rather than cell based, see e.g., [10, 11, 4]. This somehow generalizes the nodal based viscosity approach that was proposed for high order spectral element methods in [8, Sec. 4] and [9, Se. 2.4]. The advantage of the nodal based approach can be expressed with a simple argument. Let us consider a one-dimensional mesh consisting of one element, and let us assume that there is a discontinuity within this element. For any polynomial degree, a cell-based approach yields a constant artificial viscosity which can be over dissipative, while the nodal-based definition, introduces a contribution that adds viscosity to the nodes on the discontinuity which are only located at the entropy production or jumps of the solution.

Remark 3.1. The entropy residual can also be computed using the standard finite element projection algorithm, where for given function S_h and \mathbf{u}_h , $R_h \in C^1([0, \hat{t}]; \mathcal{X}_h)$ is sought such that

$$(R_h, v) = (|\partial_t S_h + \nabla \cdot (\mathbf{u}_h S_h)|, v), \quad \forall v \in \mathcal{X}_h. \quad (20)$$

The left-hand side of this problem consists of a mass matrix which is assembled only once. The matrix can be lumped to accelerated the resolution of the linear system corresponding to Problem (20). The jump contribution of the entropy residual can also be computed in a similar fashion.

Remark 3.2. The time derivative of the entropy functional in (14) being approximated using a Backward Differentiation Formula (BDF) of order s [26], then the residual is approximated with an order $O(\Delta t^s + h^{p+1})$ in smooth regions. Consequently viscosity terms are of order $O(h^2 \Delta t^s + h^{p+3})$ in smooth region as h^2 is multiplied to the residual. For example, in the case of space discretization by \mathbb{P}_1 elements and an approximation by a second-order BDF of entropy residual's time derivative, viscosity terms are fourth order accurate, i.e., $O(h^4)$. In the vicinity of shocks and discontinuities the entropy residual has jump of size h^{-1} , so that the resulting entropy viscosity scales the same magnitude as the first order viscosity (17). By the definition of μ_h and κ_h , the upper bound of entropy viscosity is always first order, i.e., $O(h)$.

3.5. Time-stepping

Time-stepping is performed with an explicit third order Strong Stability Preserving Runge–Kutta scheme [27]. The r -stage explicit Runge–Kutta method for (13) is defined as:

$$\mathbf{U}_h^{n+1} = \mathbf{U}_h^n + \Delta t_n (b_1 \mathbf{K}_1 + b_2 \mathbf{K}_2 + \dots + b_r \mathbf{K}_r), \quad (21)$$

where coefficients b_i are obtained from the Butcher tableau and \mathbf{K}_i is recursively computed by solving a mass matrix linear system at each step. Provided that viscosity $\mu_i = \mu_h^n(\mathbf{U}_h^n, \mathbf{U}_h^{n-1})$ or possibly $\mu_i = \mu_h^n(\mathbf{U}_h^n, \mathbf{U}_h^{n-1}, \mathbf{U}_h^{n-2})$ if a second-order BDF is used in (14), is computed at time t^n , $\mu_h^0 = 0$, and that \mathbf{W}_l is the solution at the l -th stage of Runge–Kutta method, \mathbf{K}_l is computed as follows

$$\mathbb{M} \mathbf{K}_l = F(\mathbf{W}_l, \mu_l), \quad i = 1, 2, \dots, r. \quad (22)$$

The mass matrix is symmetric positive definite and it is assembled once, while the right-hand side vector for computing \mathbf{K}_i is assembled at every stage. In our computation, a Krylov method (GMRES) is used for solving the mass system, preconditioned with a block Jacobi method. Viscosity coefficients can also be computed at each Runge–Kutta stage as discussed in [28]: in that case $\mu_l = \mu_h^n(\mathbf{W}_l, \mathbf{W}_{l-1})$, $\mathbf{W}_0 = \mathbf{U}_h^n$.

For a given CFL number, the timestep is computed as

$$\Delta t_n = \text{CFL} \min_{N_i \in \mathcal{T}_h, i=1, \dots, I} \frac{h(N_i)}{|\mathbf{u}_h(N_i, t_n)| + \sqrt{\gamma T_h(N_i, t_n)}}. \quad (23)$$

where $h(N_i)$ is the above-defined mesh-size.

3.6. Comparison between Navier–Stokes and Guermond–Popov fluxes

This section aims at comparing the numerical performance between the usual Navier–Stokes fluxes and Guermond–Popov fluxes. Since both fluxes have similar complexity, not noticeable difference with respect to computational time has been observed. Below, are considered three main waves when solving compressible Euler equations: shock, contact line and rarefaction waves. The problem's setting is the following: the two-dimensional unit square is divided into two equal rectangles, $\Omega = [0, \frac{1}{2}] \times [0, 1] \cup [\frac{1}{2}, 1] \times [0, 1]$. The domain is filled with an ideal gas at rest with $\gamma = 1.4$, and the left and right initial states are given in Table 1 for each test cases. The wall separating two stages is removed at $t = 0$, then the computation is carried out until $t = 0.15$. Exact solutions for each problems can be found in [29, Chapter 4.].

The simulation is done using \mathbb{P}_1 finite elements on four different meshes composed of $80 \times 10, \dots, 640 \times 10$ mesh points. The slip boundary condition is imposed on all boundaries. The first order viscosities used for the construction of Navier–Stokes and Guermond–Popov fluxes, i.e., is equivalent to setting $c_{\text{ent}} = +\infty$. Moreover the following control parameters are set: CFL number is 0.3; the artificial Prandtl number is $\mathcal{P} = 1$; the parameter of the first-order viscosity is $c_{\text{max}} = 0.5$.

In our comparison, a slightly modified version of the flux in (5) was used, where an additional viscosity term $\mathcal{P}_\rho \mu_h \nabla \rho$ with artificial density Prandtl number $\mathcal{P}_\rho = 0.2$, see e.g., [9, 4], is added to the mass equation. The original Navier–Stokes fluxes are then obtained by setting $\mathcal{P}_\rho = 0$. The results of comparison are collected in Figure 1. The

Table 1: Initial condition for single wave problems

Test	ρ_L	\mathbf{u}_L	p_L	ρ_R	\mathbf{u}_R	p_R
shock	0.265574	(0.927452, 0)	0.30313	0.125	(0, 0)	0.1
contact	0.426319	(0.927452, 0)	0.30313	0.265574	(0.927452, 0)	0.30313
rarefaction	1	(0, 0)	1	0.426319	(0.927452, 0)	0.30313

first row of the figure corresponds to the single contact line, the second row corresponds to the single shock and the last row corresponds to the single rarefaction test case. Furthermore, the first column is result obtained using the original Navier–Stokes fluxes with $\mathcal{P}_\rho = 0$, the second column is using the Navier–Stokes fluxes with $\mathcal{P}_\rho = 0.2$, and finally the last column corresponds to solution obtained by Guermond–Popov fluxes. It is obvious that the worse solution is obtained with standard Navier–Stokes fluxes with zero viscosity in the mass equation. This solution is improved by adding viscosity to the density, however as the theory predicted the Navier–Stokes fluxes are not compatible with contact lines: there are some wiggles in the solution, which is absent in the Guermond–Popov case.

One can observe a small dip which develops after the shock and rarefaction waves for both Navier–Stokes and Guermond–Popov results. This is exactly the same behavior that was observed recently in [30, pages 2486-2487]. Even though these solutions are not monotone, the invariant domain property of solutions of Guermond–Popov fluxes are guaranteed, see e.g., [30], while similar proof cannot be obtained for Navier–Stokes fluxes. This latter fact points out that for system of conservation laws the concept of invariant domain property is different than monotonicity. Nonetheless, a noticeable improvement can be seen in the Guermond–Popov solution of the rarefaction test.

In conclusion, the physical Navier–Stokes fluxes with zero viscosity in the mass equation produce the worse result for all waves. Adding a small viscosity to the mass on the top of Navier–Stokes fluxes improves the solution, but not to the extent of the Guermond–Popov regularization. Finally, the proposed viscosity predicts correctly the position of the waves with respect to the reference solution.

4. Boundary conditions for the Euler system

Applying boundary conditions for the Euler system of gas dynamics is a non-trivial task, see for example [31, Chap. 11.6] and [32, Chap. 12]. Detailed discussion on implementation of characteristics boundary conditions for finite element approximation of Euler system can be found here [33]. In this section, details on the implementation of the so-called slip boundary conditions with continuous finite elements are provided: the complexity of such implementation is further turned into a nontrivial task when solving the problem in complex geometries with arbitrary polynomial degrees. Most examples provided below stand in the supersonic regime: for the channel flow case the Dirichlet boundary condition is set accordingly at the inlet, and in all cases no boundary condition is applied at the outlet, since all characteristics point outwards at the outflow boundary.

4.1. Slip boundary condition

The slip boundary condition, or sometimes it is also called *an impermeability boundary condition*, consists in only requiring non-penetration of the fluid in solid boundaries, such that the normal component of the velocity vanishes at the boundary Γ_{wall} :

$$\mathbf{u} \cdot \mathbf{n} = 0, \quad \text{on } \Gamma_{\text{wall}} \times (0, T). \quad (24)$$

This condition implies that no mass or other convective flux can go through the boundary. This boundary condition is also sometimes called reflecting boundary condition since it is known to reflect shock waves.

The slip boundary condition can be imposed either weakly in the finite element variational formulation by adding a penalty term or Lagrange multiplier to the system or enforced strongly by modifying the assembled linear system. The implementation details of these two techniques are discussed below.

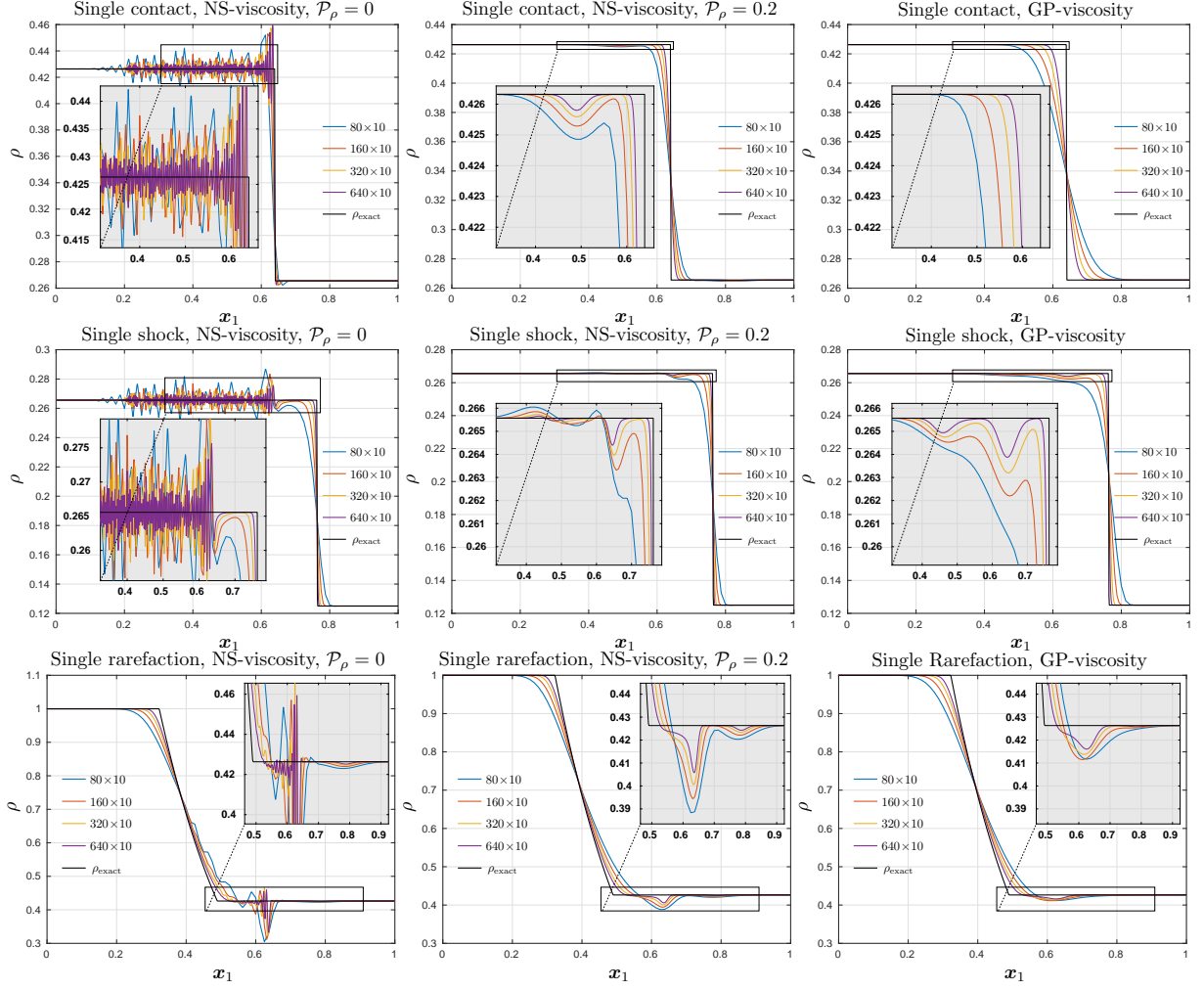


Figure 1: Three single wave Riemann problems: \mathbb{P}_1 finite element approximation of the density using different mesh resolution using Navier–Stokes and Guermond–Popov fluxes.

4.1.1. Weak slip boundary condition

The slip boundary condition is enforced weakly in the same fashion as in [17, 18] by modifying a boundary integral in the momentum equation. More precisely, the weak form of the discrete form of the momentum is written as follows:

$$\int_{\Omega} \mathbf{v}_h \cdot (\partial_t \mathbf{m}_h + \nabla \cdot (\mathbf{u}_h \otimes \mathbf{m}_h + p_h \mathbb{I})) \, d\Omega + \int_{\Gamma_{\text{wall}}} \alpha^{-1} (\mathbf{u}_h \cdot \mathbf{n}) (\mathbf{v}_h \cdot \mathbf{n}) \, d\Gamma = 0, \quad \forall \mathbf{v}_h \in \mathcal{X}_h, \quad (25)$$

where $\alpha > 0$ is a constant usually referred as a penetration constant. The weak slip condition in (25) is very easy to implement with explicit time marching techniques since the boundary integral is made explicit. When $\alpha \rightarrow 0$ the solid boundary stands as a fully non-penetrable wall. However, this choice may cause some restriction to CFL number for explicit time stepping, which will be later discussed in details in this section.

4.1.2. Strong slip boundary condition

It should be noted that in the below discussion the normal and tangent vectors are defined at the finite element nodes. For example in the two-dimensional case, if the node is situated inside the facet of triangle, then the node normal is the same as the usual facet normal. However, if the node is on the edge of the facet, then weighted average

of the all neighboring facet normals gives the node normal. An algorithm for computing node normals in three space dimensions is further described in [13, pp. 20–22].

Enforcing the slip boundary condition strongly requires to do algebraic manipulations. The idea is to find the rows in the linear system corresponding to boundary nodes and recombine them linearly so as to satisfy the desired boundary condition.

Let us illustrate the process in two space dimensions and let us denote $(\mathbf{e}_1, \mathbf{e}_2)$ the canonical Cartesian basis of \mathbb{R}^2 . Let us assume that the degrees of freedom (d.o.f.) are enumerated as follows: the density d.o.f. are enumerated from 1 to I , the first Cartesian component d.o.f. of the momentum are enumerated from $1 + I$ to $2I$, the second Cartesian component d.o.f. are enumerated from $1 + 2I$ to $3I$, and the total energy d.o.f. are enumerated from $1 + 3I$ to $4I$. Assuming that no boundary condition is enforced, the system solved is exactly (22). This linear system can be re-written into the following form:

$$\begin{pmatrix} \cdots & \cdots & \cdots & \cdots & \cdots \\ \cdots & \mathbb{M}_{i+I,i+I} & \cdots & \mathbb{M}_{i+I,i+2I} & \cdots \\ \cdots & \cdots & \cdots & \cdots & \cdots \\ \cdots & \mathbb{M}_{i+2I,i+I} & \cdots & \mathbb{M}_{i+2I,i+2I} & \cdots \\ \cdots & \cdots & \cdots & \cdots & \cdots \end{pmatrix} \cdot \begin{pmatrix} \cdots \\ m_i^1 \\ \cdots \\ m_i^2 \\ \cdots \end{pmatrix} = \begin{pmatrix} \cdots \\ F_{i+I} \\ \cdots \\ F_{i+2I} \\ \cdots \end{pmatrix}, \quad (26)$$

where the nodal values of \mathbf{K}_l at the boundary node N_i are $(\rho_i, m_i^1, m_i^2, E_i)$ with the convention that $\mathbf{m}_h(N_i) := \mathbf{m}_i = m_i^1 \mathbf{e}_1 + m_i^2 \mathbf{e}_2$. The two momentum equations at the node N_i can also be re-written

$$\int_{\Omega} \phi_i \mathbf{m} \cdot \mathbf{e}_1 \, d\Omega = F_{i+I}, \quad \int_{\Omega} \phi_i \mathbf{m} \cdot \mathbf{e}_2 \, d\Omega = F_{i+2I}. \quad (27)$$

But the condition to be enforced reads

$$m_i^1 n_i^1 + m_i^2 n_i^2 = 0, \quad \text{and} \quad \tau_i^1 \int_{\Omega} \phi_i \mathbf{m} \cdot \mathbf{e}_1 \, d\Omega + \tau_i^2 \int_{\Omega} \phi_i \mathbf{m} \cdot \mathbf{e}_2 \, d\Omega = \tau_i^1 F_{i+I} + \tau_i^2 F_{i+2I}, \quad (28)$$

where $\mathbf{n}_i := n_i^1 \mathbf{e}_1 + n_i^2 \mathbf{e}_2$ and $\tau_i := \tau_i^1 \mathbf{e}_1 + \tau_i^2 \mathbf{e}_2$ are the exterior normal and tangent vectors at N_i , respectively. As a result, after assembling \mathbb{M} without taking care of the boundary conditions, we construct the following modified mass matrix \mathbb{M}' :

$$\mathbb{M}' := \begin{pmatrix} \cdots & \cdots & \cdots & \cdots & \cdots \\ \cdots & n_i^1 & \cdots & n_i^2 & \cdots \\ \cdots & \cdots & \cdots & \cdots & \cdots \\ \cdots & \mathbb{M}'_{i+2I,i+I} & \cdots & \mathbb{M}'_{i+2I,i+2I} & \cdots \\ \cdots & \cdots & \cdots & \cdots & \cdots \end{pmatrix}, \quad (29)$$

where

$$\mathbb{M}'_{i+2I,j} = \tau_i^1 \mathbb{M}_{i+I,j} + \tau_i^2 \mathbb{M}_{i+2I,j}, \quad I + 1 \leq j \leq 3I \quad (30)$$

and instead of solving (26), the considered equation reads

$$\mathbb{M}' \cdot \begin{pmatrix} \cdots \\ m_i^1 \\ \cdots \\ m_i^2 \\ \cdots \end{pmatrix} = \begin{pmatrix} \cdots \\ 0 \\ \cdots \\ F'_{i+2I} \\ \cdots \end{pmatrix}, \quad \text{with} \quad F'_{i+2I} := \tau_i^1 F_{i+I} + \tau_i^2 F_{i+2I}. \quad (31)$$

The computation of the modified mass matrix \mathbb{M}' is done only once in a pre-processing step: first $F(\mathbf{W}_l, \mu_l)$ is computed at every Runge–Kutta sub-step, $1 \leq l \leq r$, then F is modified into F' as above to account for the slip boundary condition, and the linear system $\mathbb{M}' \mathbf{K}_l = F'(\mathbf{W}_l, \mu_l)$ is solved.

Remark 4.1. The exterior normal at N_i is unambiguously defined when the boundary is smooth at N_i , both in two and three space dimensions. The normal is defined by averaging when the boundary is not smooth at N_i . A detailed description of computation of nodal normals is given in [18].

Remark 4.2. The above discussed technique of applying the strong-slip condition can easily be applied for incompressible Navier–Stokes equations. Depending on time-marching scheme used to approximate the Navier–Stokes equations, the matrix \mathbb{M} can be any arbitrary matrix, i.e., not necessarily the mass matrix.

Remark 4.3. Dirichlet boundary conditions are enforced strongly the same way as the slip boundary conditions are implemented. In this case, each row of \mathbb{M} corresponding to a Dirichlet node is set to zero and a 1 is put on the diagonal; the right-hand side vector F is modified by assigning the corresponding Dirichlet value at the corresponding location.

4.1.3. Comparison of the weak and strong formulations

As discussed in [18], when $\alpha \rightarrow 0$, the boundary condition corresponds to full slip, i.e., no penetration over the boundary, whereas $\alpha \rightarrow \infty$ corresponds to full penetration condition. Therefore, in computational examples described in [18] the weak slip boundary condition is used by setting $\alpha = 10^{-12}$. However, our experience shows that smaller α results in severe time-step restriction for explicit RK methods. For instance $\alpha = 10^{-1}$ reduces the CFL to 0.04, and $\alpha = 10^{-2}$ reduces the CFL to 0.004, etc.

To illustrate the difference between the weak and strong slip boundary conditions, let us consider the following two-dimensional supersonic flow with a Mach number $M = 2$ past a circular cylinder of radius 0.075, for which the slip boundary condition is analyzed at boundary of the cylinder. The weak slip boundary case, depicted at the left and middle panels of Figure 2, is performed with two set of parameters, $\alpha = 1$ and $\alpha = 10^{-1}$, which correspond to $\text{CFL} = 0.4$ and $\text{CFL} = 0.04$ respectively, while the strong slip boundary condition case is computed with $\text{CFL} = 0.4$, illustrated at the right panel of Figure 2.

In the case of weak enforcement of the condition with not small enough values of α , the flow penetrates over the boundary and the sonic line or the normal shock position (plotted as a dark line) is incorrectly located. As α decreases the flow profile tends to the result obtained with the strong slip condition, but imposes a decrease of the CFL number. On the contrary, no restriction on the CFL number has been observed while solving the Euler system using the strong-slip condition. Therefore, the rest of computational results in this paper are performed using only strong-slip condition.

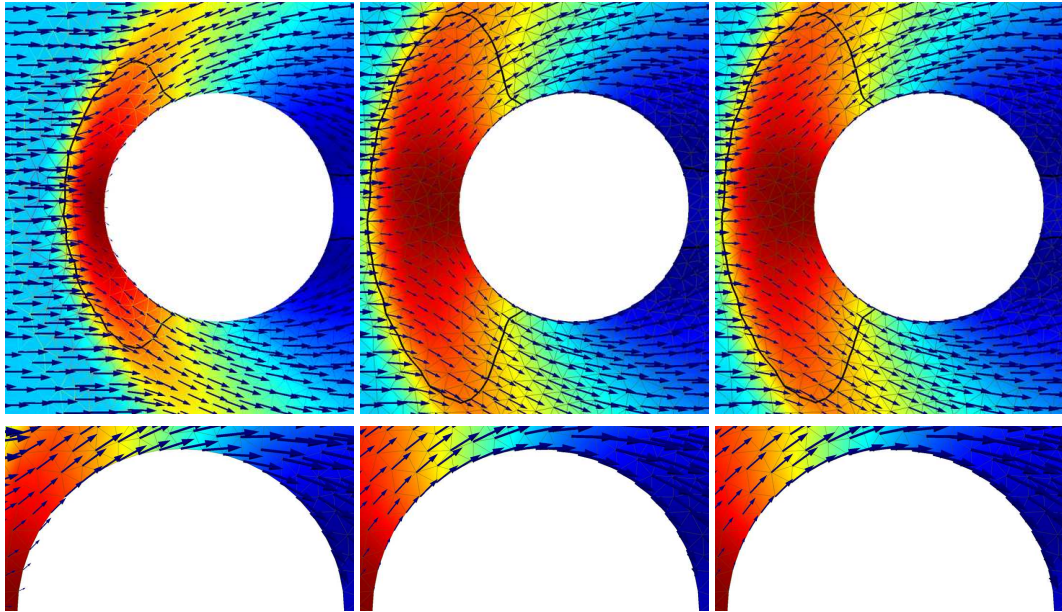


Figure 2: Supersonic Mach 2 flow around a circular cylinder. Comparison between weak and strong formulation of slip boundary condition: weak slip with $\alpha = 1$, $\text{CFL} = 0.4$ at the left panel, weak slip with $\alpha = 10^{-1}$, $\text{CFL} = 0.04$ at the middle panel, strong slip with $\text{CFL} = 0.4$ at the right panel. The lower row is a zoom close to the upper side of the cylinder. The sonic line $M = 1$ is plotted in black.

5. Numerical tests

Let us consider the following standards 1D and 2D benchmarks for compressible Euler equations. Firstly, the presented method is applied to solve the Sod shock-tube problem, where the exact solution is known. Secondly, two well-known 2D step configurations are considered: the forward facing step in a wind tunnel and the double Mach reflection problem. Thirdly, two tests cases involving almost all features of compressible flows are investigated: an external supersonic flow around a circular cylinder, and an explosion problem in 2D, in a domain with eight circular cylinders which both exhibit bow and attached shocks, rarefaction waves, contact lines, triple shock, Mach stem, and oscillatory wake in the downstream. Finally, the well-known shock-bubble interaction problem is presented to illustrate high-accuracy of the method.

The implementations are based on the open-source finite element software of the FEniCS project [24], and are fully parallel while being independent on the number of space dimensions or the polynomial degree of the approximation. We refer the reader to [34, 35] where some parallel performance analysis of the FEniCS project is done for linear polynomial spaces by solving problems from continuum mechanics.

The dependent variables are normalized as follows: L being the reference length scale, the density ρ , velocity \mathbf{u} and temperature T are normalized by their free stream values ρ_∞, u_∞ and T_∞ . The time, pressure, energy and velocity are normalized by $L/u_\infty, \rho_\infty u_\infty^2, u_\infty^2$ and u_∞ , respectively. Furthermore, a reference Mach number is defined as $M = u_\infty/c_\infty$, where c_∞ is a reference value of the speed of sound. The control parameters in the entropy viscosity for the below test cases are collected in Table 2.

Table 2: The control parameters used in entropy viscosity

Tests	Time-stepping	CFL	c_{\max}	c_{ent}	\mathcal{P}	Time
Sec. 5.1	RK4	0.3	0.25	1	0.4	1.00
Sec. 5.2	SSP-RK3	0.3	0.25	1	0.4	0.25
Sec. 5.3	SSP-RK3	0.3	0.25	1	1.0	0.25
Sec. 5.4	SSP-RK3	0.4	0.25	1	0.4	4.00
Sec. 5.5	SSP-RK3	0.4	0.25	1	0.4	0.20
Sec. 5.6	SSP-RK3	0.3	0.25	1	0.4	5.00
Sec. 5.7	SSP-RK3	0.3	0.25	1	0.4	4.25
Sec. 5.8	SSP-RK3	0.3	0.25	1	0.4	0.70

5.1. Accuracy test

Let us consider the unit square domain $\Omega = (0, 1) \times (0, 1)$ with periodic boundary condition in all boundaries. The numerical approximation of the following exact smooth solution,

$$\rho(t, x, y) = 1 + 0.2 \sin(2\pi(x + y - 2t(u_1 + u_2))), \quad (32)$$

is computed, with $u_1 = \frac{5}{2}, u_2 = -\frac{1}{2}$, and pressure is defined as $p = 1$. The solution is a periodic wave traveling to right-lower direction. The problem is solved until $t = 1$, so that the wave is allowed to make one full rotation. The standard Galerkin finite elements and entropy viscosity stabilization are compared for different polynomial spaces. In all cases time-stepping is performed with a fourth order Runge–Kutta method.

The results of the simulation are collected in Table 3 and Figure 3. The rate for \mathbb{P}_2 is better than Galerkin rate, however it seems to be still sub-optimal. Similar behavior has been mentioned in [9]. In the figure h_K/N denotes the cell diameter h_K divided to the polynomial degree N . Therefore, this quantity defines the number of degrees of freedom for each finite element spaces. For fixed degrees of freedom, the magnitude of the error decreases when polynomial order increases.

5.2. Sod shock-tube problem

In this section the Sod shock-tube problem is solved in two space dimensions. The problem setting is the following: the two-dimensional unit square is divided into two equal rectangles, $\Omega = [0, \frac{1}{2}] \times [0, 1] \cup [\frac{1}{2}, 1] \times [0, 1]$. The domain

Table 3: Convergence tests for entropy viscosity and Galerkin solutions with respect to exact smooth solution (32) at time $t = 1$.

h_K/N	\mathbb{P}_1 Entropy Viscosity				\mathbb{P}_1 Galerkin			
	L^1	rate	L^2	rate	L^1	rate	L^2	rate
0.025	7.32e-02	—	8.19e-02	—	3.17e-03	—	3.84e-03	—
0.0125	1.22e-02	2.58	1.49e-02	2.46	7.85e-04	2.01	9.54e-04	2.01
0.00625	1.94e-03	2.65	2.32e-03	2.69	1.96e-04	2.00	2.39e-04	2.00
0.003125	3.15e-04	2.62	3.61e-04	2.69	4.91e-05	2.00	5.97e-05	2.00
0.0015625	4.63e-05	2.77	5.27e-05	2.77	1.23e-05	2.00	1.49e-05	2.00

h_K/N	\mathbb{P}_2 Entropy Viscosity				\mathbb{P}_2 Galerkin			
	L^1	rate	L^2	rate	L^1	rate	L^2	rate
0.025	1.15e-02	—	1.28e-02	—	7.09e-03	—	8.25e-03	—
0.0125	1.87e-03	2.62	2.10e-03	2.61	1.87e-03	1.92	2.19e-03	1.91
0.00625	3.18e-04	2.55	3.66e-04	2.52	4.72e-04	1.99	5.52e-04	1.99
0.003125	5.77e-05	2.46	7.05e-05	2.38	1.20e-04	1.97	1.39e-04	1.99
0.0015625	1.35e-05	2.10	1.66e-05	2.09	3.02e-05	1.99	3.48e-05	2.00

h_K/N	\mathbb{P}_3 Entropy Viscosity				\mathbb{P}_3 Galerkin			
	L^1	rate	L^2	rate	L^1	rate	L^2	rate
0.033333	9.56e-03	—	1.05e-02	—	7.82e-04	—	1.51e-03	—
0.016667	5.80e-04	4.04	6.70e-04	3.97	4.39e-05	4.15	9.29e-05	4.03
0.008333	4.24e-05	3.77	5.48e-05	3.61	4.38e-06	3.33	8.82e-06	3.40
0.004167	2.86e-06	3.89	4.16e-06	3.72	3.64e-07	3.59	1.36e-06	2.70
0.002083	3.32e-07	3.11	4.65e-07	3.16	3.36e-07	0.11	4.14e-07	1.71

h_K/N	\mathbb{P}_4 Entropy Viscosity				\mathbb{P}_4 Galerkin			
	L^1	rate	L^2	rate	L^1	rate	L^2	rate
0.025	1.85e-03	—	2.06e-03	—	2.97e-04	—	8.34e-04	—
0.0125	4.91e-05	5.24	6.15e-05	5.07	4.19e-06	6.15	1.41e-05	5.89
0.00625	2.34e-06	4.39	2.92e-06	4.40	3.35e-07	3.64	6.75e-07	4.38
0.003125	3.11e-07	2.91	4.08e-07	2.84	2.43e-07	0.46	3.24e-07	1.06
0.0015625	6.51e-08	2.26	9.14e-08	2.16	2.62e-07	-0.11	3.32e-07	-0.04

is filled with an ideal gas at rest with $\gamma = 1.4$, and the left and right initial states are $\rho_L = 1$, $\mathbf{u}_L = (0, 0)$, $p_L = 1$, and $\rho_R = 0.125$, $\mathbf{u}_R = (0, 0)$, $p_R = 0.1$.

The divider separating the two chambers is removed at $t = 0$. The exact solution consists of a rarefaction fan, followed by a contact discontinuity, and a shock wave. The simulation is performed until $t = 0.25$ on five different meshes, and using \mathbb{P}_1 , \mathbb{P}_2 , \mathbb{P}_3 and \mathbb{P}_4 finite element approximations: 40×10 , 80×10 , \dots , 640×10 . The slip boundary condition is imposed on all boundaries. The same set of parameters was used for all the meshes: CFL number 0.4; the artificial Prandtl number $\mathcal{P} = 0.7$; the parameter of the first-order viscosity is $c_{\max} = 0.3$, and for the entropy viscosity $c_{\text{ent}} = 1.0$.

The convergence history of \mathbb{P}_1 polynomial approximations against the exact density and temperature at the final time $t = 0.25$ is collected in Figure 4. Corresponding magnitude of entropy viscosity throughout the computation is plotted in Figure 5. Most of the amount of viscosity is added in the shock region, since the entropy residual approaches to a Dirac measure supported in the shock. Due the jump term used in the definition of the viscosity, significant amount of dissipation is added in the contact line. Therefore, the contact line is rather diffuse for coarser meshes, however it improves when the mesh is refined. Some undershoot can be noticed in the temperature profile after the shock. This overshoot can be improved by changing the values of control parameters in the artificial diffusion, see e.g., [8]. Figures 4 and 5 are obtained along the cut line over $x_2 = 0.5$.

In Figure 6 convergence history in L^1 and L^2 norms is collected together with corresponding theoretical values 1 and $1/2$ respectively, see e.g., [36]. While increasing the polynomial degree improves both rates, it is clearer for the L^1 -norm. The mean value of the L^1 and L^2 norms for each variable and polynomial degrees is reported in Table 4, which is obtained by taking the arithmetic mean of the rates obtained from the sequenced refined meshes. Here again, the mean value of the L^1 -norm improves towards the theoretical value 1 for higher polynomial degrees. The values of the L^2 -norm are around theoretical value $1/2$ for density and momentum, while it is a bit high for the energy.

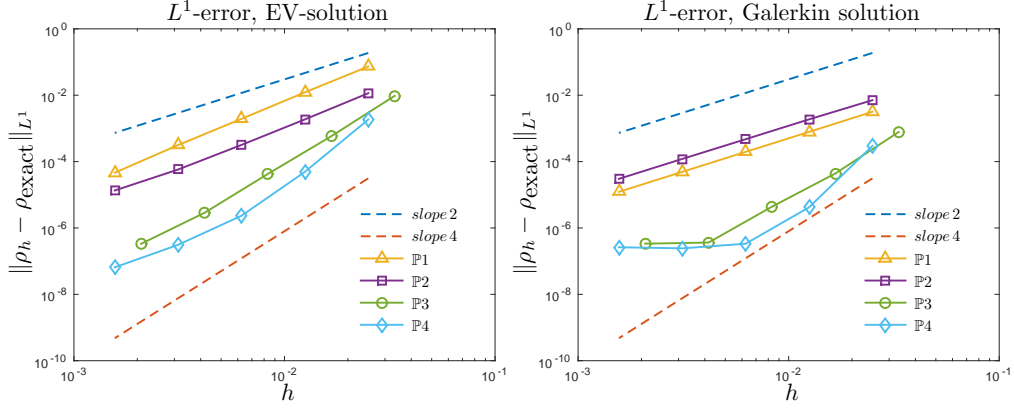


Figure 3: Accuracy test: convergence history for density ρ with respect to smooth exact solution (32).

Table 4: Mean value of the convergence rates of the L^1 and L^2 norms for EV-solution

Degree	L^1 -rate			L^2 -rate		
	ρ	m	E	ρ	m	E
P1	0.8318	0.8103	0.9407	0.5878	0.4979	0.7269
P2	0.8237	0.8031	0.9048	0.5770	0.5089	0.7118
P3	0.8838	0.8591	0.9401	0.5637	0.4558	0.6039
P4	0.9182	0.9150	0.9524	0.6205	0.5618	0.7314

5.3. 2D Riemann problem

In this test, a two-dimensional Riemann problem is considered, as defined in case #12 of [37]. The problem is solved on the unit square $\Omega = (0, 1) \times (0, 1)$. The gas constant is set $\gamma = 1.4$ and the initial condition is defined as

$$\begin{aligned}
 \rho &= 4/5, & p &= 1, & \mathbf{u} &= (0, 0) & \text{in } 0 < x < 0.5, & 0 < y < 0.5, \\
 \rho &= 1, & p &= 1, & \mathbf{u} &= (1/\sqrt{17}, 0) & \text{in } 0 < x < 0.5, & 0.5 < y < 1, \\
 \rho &= 1, & p &= 1, & \mathbf{u} &= (0, 1/\sqrt{17}) & \text{in } 0.5 < x < 1, & 0 < y < 0.5, \\
 \rho &= 17/32, & p &= 2/5, & \mathbf{u} &= (0, 0) & \text{in } 0.5 < x < 1, & 0.5 < y < 1.
 \end{aligned} \tag{33}$$

The initial condition consists of two contact lines (lower left – upper left and lower left – lower right), and two shocks (upper left – upper right and upper right – lower right).

The problem is solved until $t = 0.25$ using 100×100 mesh points on \mathbb{P}_4 finite element approximation, which results to 400×400 \mathbb{P}_4 nodes and is the same mesh resolution is used in [37]. The left panel of Figure 7 describes density contours, pressure color-map and velocity arrows. The contact line on the lower left quadrant is resolved accurately, the shocks and the fine structures behind the shocks are captured well. This solution compares well with the finite difference solution presented in the reference [37]. The right panel of Figure 7 plots the magnitude of entropy viscosity μ . One can see that the viscosity is active in the vicinity of shocks and contact lines.

5.4. Wind tunnel with a forward-facing step

This case of a Mach $M = 3$ flow in a two-dimensional wind tunnel with a step, was originally introduced by Emery in [38], and is a well known benchmark used for testing new methods since Woodward and Collela [39]. The wind tunnel with length 3.0 and height 1.0 contains a step with height 0.2, situated at a distance 0.6 from the inflow. The initial data for the problem is $\rho = 1.4, m = (4.2, 0), E = 8.8$. In order to avoid the nonphysical effect caused by the singularity point, the corner was rounded off as suggested in [13] with a relatively small fixed curvature of radius 0.0025, see Figure 8. The slip boundary condition is enforced on the wall boundaries, no physical boundary condition is needed at the outflow. Figure 9 presents the computation results for two different meshes: a coarse mesh with $h_K \approx 0.025$, and a fine mesh with $h_K \approx 0.008$ using \mathbb{P}_1 and \mathbb{P}_2 finite element approximations. The left panels of the figure describes 30 contours of the density and the right panels plot the magnitude of the entropy viscosity.

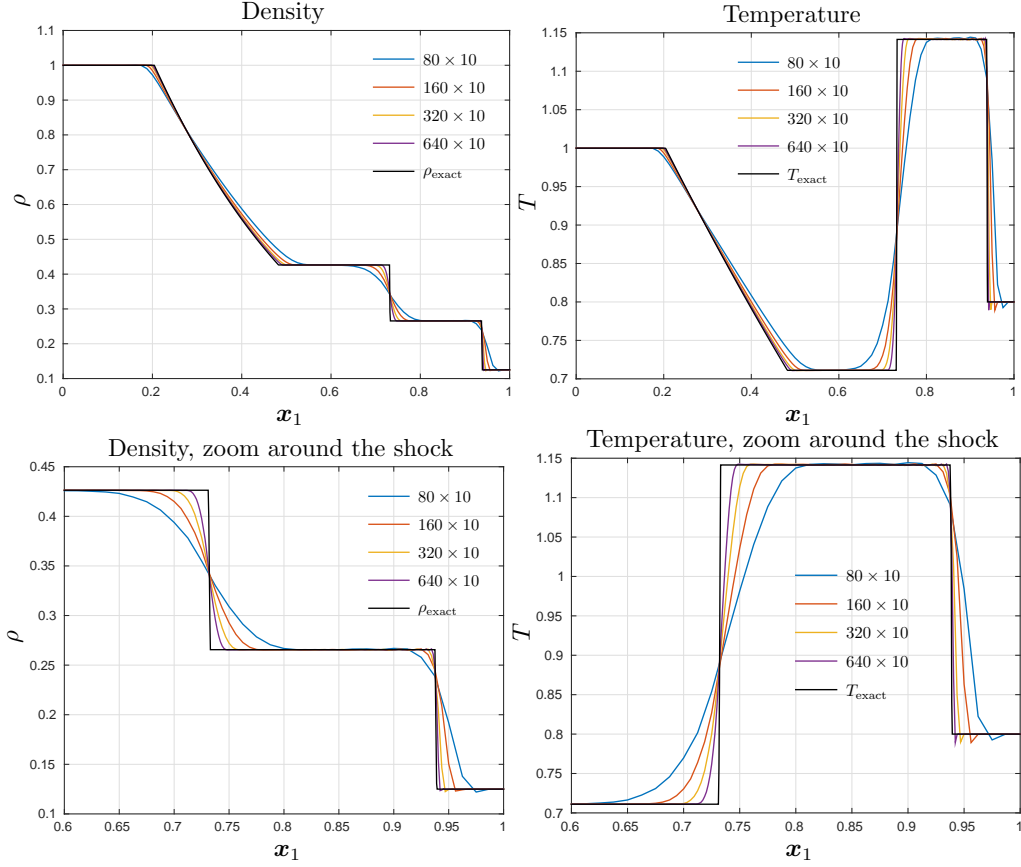


Figure 4: Sod shock-tube problem: comparisons of exact density, at the left panels, and temperature, at the right panels, for \mathbb{P}_1 polynomials at $t = 0.25$.

Usually this simulation is done until time $t = 4$. After hitting the step, the flow creates a strong bow shock, which travels toward the upper boundary. Later, the shock is reflected, creates a Mach stem and travels to the lower boundary, and so on. Behind the upper Mach stem, attached to the triple point where the shocks meet, the physical solution has a contact discontinuity or the so-called Kelvin–Helmholtz instability. Usually, it is very difficult to capture this instability numerically. Low order methods dissipate too much along this line, therefore the instability remains invisible. However, this path is already captured on the coarsest mesh, and becomes more visible on finer meshes.

5.5. Two-dimensional double Mach reflection

In this section, the so-called double Mach reflection problem, popularized by Woodward and Collela [39], is studied. An incident Mach 10 shock wave of the ideal gas, $\gamma = 1.4$, enters to two-dimensional wind tunnel with a wedge with 30 degree angle. Initially the value of the density is 1.4 and the pressure is set to 1. This problem is usually solved until $t = 0.2$. The computation is performed on two meshes: a coarse mesh with mesh-size $h_K \approx 0.025$ and a fine mesh with mesh-size $h_K \approx 0.0025$. In both simulations second order polynomial degrees \mathbb{P}_2 are used. To make all the features of the solution visible Schlieren gray-scale diagram [40, page 793] are plotted,

$$\sigma = \exp\left(-\beta \frac{|\nabla z| - \min_{\Omega} |\nabla z|}{\max_{\Omega} (|\nabla z|) - \min_{\Omega} |\nabla z|}\right),$$

with $\beta = 10$ and z the vertical momentum, i.e., $z = m_2$.

After hitting the wedge, the flow develops several strong shock waves and separates fluid into several flow regions. The incident shock gets reflected and creates a Mach stem attached to the boundary of the wedge. This Mach stem

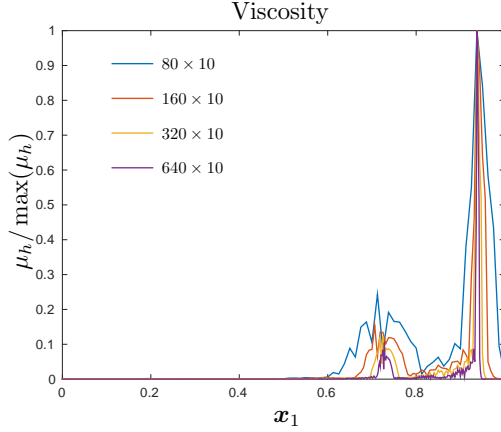


Figure 5: Sod shock-tube problem: the scaled magnitude of \mathbb{P}_1 entropy viscosity.

together with the incident and reflected shock waves create the first triple point which is very well visible even for the coarse mesh, see left panel of Figure 10. Then, the reflected shock wave breaks into the bowed shock attached to the leading edge of the wedge and the secondary reflected shock. They form the second triple point. There are two slip lines developed from the triple points. The first slip line is rather strong and clearly visible even in the coarse mesh. It hits the secondary reflected shock and forms a sliding curved flow structure that moves behind the Mach stem. As it was reported earlier in [39], the Kelvin–Helmholtz instabilities develop along this line which is only possible to capture with high resolution schemes. However, the second slip line from the secondary triple point remains as the main challenge for numerical schemes. This line is barely visible in our computation at the coarse mesh, but it well captured in the fine mesh.

5.6. Supersonic flow around circular cylinder

Let us consider a circular cylinder with diameter 0.125 centered at point $(0.3, 0.25)$ in a two-dimensional wind tunnel with size $(x_1, x_2) \in [0, 2] \times [0, 0.5]$. The initial values are given as $\rho = 1.4, p = 1, \mathbf{u} = 0$, and boundary conditions consist of Dirichlet at inflow, slip at the walls and on the cylinder. No boundary condition is applied at the outflow. Computational results are presented on two meshes, see e.g. Figure 11: a coarse mesh with mesh size $h_K \approx 0.01$ which has 26,626 vertices and 52,612 triangles, and a finer mesh with mesh size $h_K \approx 0.006$ that has 64,020 vertices and 127,068 triangles. The \mathbb{P}_1 finite elements is used in the coarse mesh and \mathbb{P}_2 finite elements is used in the fine mesh, that results 26,626 and 508,272 finite element nodes in each cases respectively.

The supersonic flow of Mach 2 enters to the domain from the left boundary. After hitting the cylinder a strong bow shock develops in front of the cylinder and travels towards the upper and lower walls. Two other attached oblique shocks appears on the downstream boundary of the cylinder, that travels towards outflow. These two shocks are well captured in both coarse and fine meshes. Another shock, which is usually referred as a “fishtail” shock, is visible behind the cylinder in results for times $t = 0.5$ and $t = 0.7$ only for the fine mesh. This shock needs high accuracy in the numerical computation in order to be well resolved. Later, the bow and oblique shocks reflects from the upper and lower boundaries and solutions for both meshes look alike up to time $t = 2$.

The flow separates at the points of the cylinder’s boundary where the oblique shock starts and a small recirculating region appears on the back of the cylinder. It is visible already at $t = 0.15$ only in the fine mesh. Another flow feature that is not resolved on the coarse mesh is a long run trailing vortex which usually starts after recirculating region. The vortex has a very complex feature and has unpredictable behavior with very small scale fluctuations.

Due to lower resolution in the computation, besides the strong shock waves, the solution from the coarse mesh behaves rather different than the one from the fine mesh. For example, the coarse mesh could not capture small scales instabilities in the solution like a trailing vortex, fishtail shock wave or the contact line which develops from the triple shock points of the bow shock, Mach stems and reflected shocks, both close to upper and lower boundaries.

5.7. Explosion in a domain with cylinders

The computational domain consists of a two-dimensional circle with radius 2 centered at the origin, see Figure 12. Eight circular cylinders with radius 0.3 are placed such that their center located at 1.4 distance from the origin, and the distance between the neighbors are equal. A compressed gas with density 1 and pressure 1 is put inside a circle with radius $\sqrt{0.4}$ located at the origin. The outside density is 0.125, pressure is 0.1 and velocity is at the rest. The slip boundary condition is applied to all boundaries including the cylinder boundaries.

The mesh, rather fine and with a relative mesh-size $h_K \approx 0.0065$ accounts for 382,701 vertices and 760,792 fully unstructured triangles. The mesh-size and mesh resolution for this problem is comparable to the one used in [37, p. 1012], where they solve this problem in a square using different finite difference schemes. Second order finite element polynomials are used with a total of 1,539,650 \mathbb{P}_2 nodes. At time $t = 0$ the walls between the compressed and rested gases are taken. The circular shock is generated from the boundary of the gases and travels away from the center. After this strong shock, a circular contact line travels at the same direction as the shock but with slower speed, and a circular rarefaction wave travels towards the origin. The shock wave hits the cylinders and partially gets reflected, the other part passes between the cylinders and hits the wall of the main circle. After hitting the circle, the shock wave travels towards the origin. Again, in its way it partially gets reflected by hitting the cylinders from the other side and partially travels inward between them. On the other side, the traveling circular contact becomes weaker and at some point it rests and then travels inward towards the origin. This contact line becomes unstable and breaks down to small vortices. The circular rarefaction wave which was traveling inwards, at some points hits the origin and reflects as a rarefaction, over-expands and creates a new shock waves traveling inwards. As time evolves this shock wave reflects from the origin and travels outward, in its way it collides with the other shock ways and contact line and so on.

The Schlieren diagram of the density is presented in Figure 13 for different time levels. The method presented in this paper seems to perform equally well in capturing instabilities along the contact line. Figure 14 zoom on the solution close to the origin for later time. One can see that the magnitude of the entropy viscosity focuses only to defuse the strong discontinuities.

Detailed description of the explosion tests in two and three space dimensions in a different domain is provided in [29, Sec. 17.1, pp 602–606] and [37, Sec. 4.8].

5.8. Shock-bubble interaction

Finally, the well-known example of the interaction between a planar shock and a spherical region with a density jump across the surface is studied; see [41] for the original setup with two different gasses and to [42] for a simplified setting with one gas. This test case is usually chosen to evaluate the ability of schemes to perform turbulence simulations; it involves mixing and formation of vortices induced by the shock wave running through the heterogeneous media. The problem setting is as follows: a circle of radius 0.2 is centered at (0.3, 0) in the computational domain $[-0.2, 6] \times [0, 2]$. Since the problem is symmetric with respect to the line $y = 0$, the computational domain is chosen to be a half of the original geometry.

The gas has zero initial velocity and the pressure is initially equal to 1 everywhere. The density is set to be 0.1 inside the circle and 1 otherwise at $t = 0$. A planar single shock wave, parallel to the y -axis, starts at $x = 0$ and propagates along the x -axis. The problem is solved with three different pressures behind the shock: 2, 3 and 10, giving the shock Mach numbers $M_S = 1.3628$, $M_S = 1.6475$ and $M_S = 2.952$ respectively.

Let us denote the right state pressure and density as $p_r = 1, \rho_r = 1$. Provided that the shock Mach number M_S is given, using the formulas for the one-dimensional elementary shock wave between constant states stated in [43, page 1398] and the definition of shock Mach number in [29, page 99-103], the inflow pressure, density and velocity is set as follows:

$$p_{\text{in}} = p_r \frac{2\gamma M_S^2 - (\gamma - 1)}{\gamma + 1}, \quad \rho_{\text{in}} = \rho_r \frac{\frac{p_{\text{in}}}{p_r} + \frac{\gamma-1}{\gamma+1}}{1 + \frac{p_{\text{in}}}{p_r} \frac{\gamma-1}{\gamma+1}},$$

$$\mathbf{u}_{\text{in}} = \left(\left(\frac{(p_{\text{in}} - p_r)(\rho_{\text{in}} - \rho_r)}{\rho_{\text{in}} \rho_r} \right)^{\frac{1}{2}}, 0 \right).$$

The slip boundary condition is imposed in all other boundaries. As the region of interest lies in the square $[-0.2, 1.5] \times [0, 0.5]$, the mesh is constructed to be rather coarse outside of this area.

The computational domain is triangulated by unstructured grid with meshsize $h_K \approx 0.0035$, which results in 94,450 vertices and 182,287 triangles. Then, the second order piecewise polynomials are used to discretize the system, which corresponds to 370,388 \mathbb{P}_2 nodes. This mesh resolution is approximately the same as the one used in [44, 45], where the problem was solved using finite volume and front-tracking methods.

The density field is represented at various times in Figure 15 for all Mach regimes. The numerical solution evolves correctly through the stages described in [41] and provides the level of detail of flow structures expected for highly accurate schemes on the given mesh. To get a better view of how well small scales are resolved, the tip of the bubble is plotted for later times in Figure 16: the proposed finite element method captures the small scales very accurately as a reference finite volume approximation [44, 45].

6. Conclusion

The main aim of this paper was to investigate numerically a new class of regularization of the Euler system which was recently proposed in [15] in the context of continuous Lagrange finite element approximations. The numerical scheme considered relies on the entropy viscosity algorithm to achieved high-order in space while a third- or fourth-order Strong Stability Preserving SPP Runge–Kutta algorithm is used for the time discretization. High-order accuracy is assessed on standard two-dimensional compressible flow benchmarks.

A natural extension of this paper is to satisfy the positivity of density and internal energy in the discrete setting. While the continuous mathematical model using Guermond–Popov fluxes ensures the positivity of the unknown, this property does not hold for the corresponding continuous finite element approximations, as it may be the case with other numerical methods where an *ad hoc* discrete differential operator is constructed (limiters with finite volume and finite difference methods). Transposition of positivity properties to the discrete level can be achieved for instance by introducing a viscous bilinear form was introduced by Guermond and Nazarov [25], satisfying a discrete maximum principle for a continuous finite element approximation of a scalar conservation laws in arbitrary unstructured meshes in any space dimensions. The entropy viscosity implementation of Guermond–Popov fluxes in this paper together with the first order positivity preserving scheme can be the main two ingredients for the Boris–Book–Zalesak flux correction techniques, see e.g. [46, 47], in order to get higher order in space, as in [48]. In this perspective, the extension of the presented method to obtain a first order positivity preserving scheme to compute compressible Euler equations is a prerequisite.

Acknowledgment

This project was initiated during Murtazo Nazarov’s post-doc at Texas A&M University. Murtazo Nazarov is grateful to Jean-Luc Guermond and Bojan Popov for valuable discussions and comments during preparing this material. The authors also would like to thank the two anonymous reviewers for their careful reading of the manuscript and for their valuable suggestions and comments.

- [1] T. J. R. Hughes, M. Mallet, A new finite element formulation for computational fluid dynamics. IV. A discontinuity-capturing operator for multidimensional advective-diffusive systems, *Comput. Methods Appl. Mech. Engrg.* 58 (3) (1986) 329–336. doi:10.1016/0045-7825(86)90153-2.
URL [http://dx.doi.org/10.1016/0045-7825\(86\)90153-2](http://dx.doi.org/10.1016/0045-7825(86)90153-2)
- [2] C. Johnson, A. Szepessy, P. Hansbo, On the convergence of shock-capturing streamline diffusion finite element methods for hyperbolic conservation laws, *Mathematics of Computation* 54(189) (1990) 107–129.
- [3] M. Nazarov, Convergence of a residual based artificial viscosity finite element method, *Comput. Math. Appl.* 65 (4) (2013) 616–626. doi:10.1016/j.camwa.2012.11.003.
URL <http://dx.doi.org/10.1016/j.camwa.2012.11.003>
- [4] M. Nazarov, J. Hoffman, Residual-based artificial viscosity for simulation of turbulent compressible flow using adaptive finite element methods, *Internat. J. Numer. Methods Fluids* 71 (3) (2013) 339–357. doi:10.1002/flid.3663.
URL <http://dx.doi.org/10.1002/flid.3663>
- [5] S. Marras, M. Nazarov, F. X. Giraldo, Stabilized high-order Galerkin methods based on a parameter-free dynamic SGS model for LES, *J. Comput. Phys.* 301 (2015) 77–101. doi:10.1016/j.jcp.2015.07.034.
URL <http://dx.doi.org/10.1016/j.jcp.2015.07.034>
- [6] G. E. Barter, D. L. Darmofal, Shock capturing with PDE-based artificial viscosity for DGFEM. I. Formulation, *J. Comput. Phys.* 229 (5) (2010) 1810–1827. doi:10.1016/j.jcp.2009.11.010.
URL <http://dx.doi.org/10.1016/j.jcp.2009.11.010>
- [7] J. Reisner, J. Serencsa, S. Shkoller, A space-time smooth artificial viscosity method for nonlinear conservation laws, *J. Comput. Phys.* 235 (2013) 912–933. doi:10.1016/j.jcp.2012.08.027.
URL <http://dx.doi.org/10.1016/j.jcp.2012.08.027>
- [8] J.-L. Guermond, R. Pasquetti, Entropy-based nonlinear viscosity for Fourier approximations of conservation laws, *C. R. Math. Acad. Sci. Paris* 346 (13-14) (2008) 801–806. doi:10.1016/j.crma.2008.05.013.
URL <http://dx.doi.org/10.1016/j.crma.2008.05.013>
- [9] J.-L. Guermond, R. Pasquetti, B. Popov, Entropy viscosity method for nonlinear conservation laws, *J. Comput. Phys.* 230 (11) (2011) 4248–4267.
- [10] P. Persson, J. Peraire, Sub-Cell Shock Capturing for Discontinuous Galerkin Methods, *AIAA Aerospace Sciences Meeting and Exhibit* 44th.
- [11] V. Zingan, J.-L. Guermond, J. Morel, B. Popov, Implementation of the entropy viscosity method with the discontinuous Galerkin method, *Comput. Methods Appl. Mech. Engrg.* 253 (2013) 479–490. doi:10.1016/j.cma.2012.08.018.
URL <http://dx.doi.org/10.1016/j.cma.2012.08.018>
- [12] J.-L. Guermond, R. Pasquetti, B. Popov, From suitable weak solutions to entropy viscosity, *J. Sci. Comput.* 49 (1) (2011) 35–50. doi:10.1007/s10915-010-9445-3.
URL <http://dx.doi.org/10.1007/s10915-010-9445-3>
- [13] M. Nazarov, Adaptive algorithms and high order stabilization for finite element computation of turbulent compressible flow, Ph.D. thesis, KTH, Numerical Analysis, NA, QC 20110627 (2011).
- [14] J. L. Guermond, R. Pasquetti, Entropy viscosity method for high-order approximations of conservation laws, in: *Spectral and high order methods for partial differential equations*, Vol. 76 of *Lect. Notes Comput. Sci. Eng.*, Springer, Heidelberg, 2011, pp. 411–418. doi:10.1007/978-3-642-15337-2_39.
URL http://dx.doi.org/10.1007/978-3-642-15337-2_39
- [15] J.-L. Guermond, B. Popov, Viscous regularization of the Euler equations and entropy principles, *SIAM J. Appl. Math.* 74 (2) (2014) 284–305. doi:10.1137/120903312.
URL <http://dx.doi.org/10.1137/120903312>
- [16] M. O. Delchini, J. C. Ragusa, R. A. Berry, Entropy-based viscous regularization for the multi-dimensional Euler equations in low-Mach and transonic flows, *Comput. & Fluids* 118 (2015) 225–244. doi:10.1016/j.compfluid.2015.06.005.
URL <http://dx.doi.org/10.1016/j.compfluid.2015.06.005>
- [17] W. Layton, Weak imposition of “no-slip” conditions in finite element methods, *Comput. Math. Appl.* 38 (5-6) (1999) 129–142. doi:10.1016/S0898-1221(99)00220-5.
URL [http://dx.doi.org/10.1016/S0898-1221\(99\)00220-5](http://dx.doi.org/10.1016/S0898-1221(99)00220-5)
- [18] V. John, Slip with friction and penetration with resistance boundary conditions for the Navier-Stokes equations—numerical tests and aspects of the implementation, *J. Comput. Appl. Math.* 147 (2) (2002) 287–300. doi:10.1016/S0377-0427(02)00437-5.
URL [http://dx.doi.org/10.1016/S0377-0427\(02\)00437-5](http://dx.doi.org/10.1016/S0377-0427(02)00437-5)
- [19] A. Harten, P. D. Lax, C. D. Levermore, W. J. Morokoff, Convex entropies and hyperbolicity for general Euler equations, *SIAM J. Numer. Anal.* 35 (6) (1998) 2117–2127 (electronic). doi:10.1137/S0036142997316700.
URL <http://dx.doi.org/10.1137/S0036142997316700>
- [20] D. Serre, *Systèmes de lois de conservation. I, Fondations. [Foundations]*, Diderot Editeur, Paris, 1996, hyperbolicité, entropies, ondes de choc. [Hyperbolicity, entropies, shock waves].
- [21] A. Harten, On the symmetric form of systems of conservation laws with entropy, *J. Comput. Phys.* 49 (1) (1983) 151–164. doi:10.1016/0021-9991(83)90118-3.
URL [http://dx.doi.org/10.1016/0021-9991\(83\)90118-3](http://dx.doi.org/10.1016/0021-9991(83)90118-3)
- [22] J.-L. Guermond, M. Nazarov, B. Popov, Implementation of the entropy viscosity method, *Tech. Rep.* 4015, KTH, Numerical Analysis, NA, qC 20110720 (2011).
- [23] M. Nazarov, J. Hoffman, On the stability of the dual problem for high Reynolds number flow past a circular cylinder in two dimensions, *SIAM J. Sci. Comput.* 34 (4) (2012) A1905–A1924. doi:10.1137/110836213.
URL <http://dx.doi.org/10.1137/110836213>
- [24] A. Logg, K.-A. Mardal, G. N. Wells, et al., *Automated Solution of Differential Equations by the Finite Element Method*, Springer, 2012.

- doi:10.1007/978-3-642-23099-8.
- [25] J.-L. Guermond, M. Nazarov, A maximum-principle preserving C^0 finite element method for scalar conservation equations, *Comput. Methods Appl. Mech. Engrg.* 272 (2014) 198–213. doi:10.1016/j.cma.2013.12.015.
URL <http://dx.doi.org/10.1016/j.cma.2013.12.015>
 - [26] E. Süli, D. F. Mayers, *An introduction to numerical analysis*, Cambridge University Press, Cambridge, 2003. doi:10.1017/CB09780511801181.
URL <http://dx.doi.org/10.1017/CB09780511801181>
 - [27] S. Gottlieb, C.-W. Shu, E. Tadmor, Strong stability-preserving high-order time discretization methods, *SIAM Rev.* 43 (1) (2001) 89–112 (electronic). doi:10.1137/S003614450036757X.
URL <http://dx.doi.org/10.1137/S003614450036757X>
 - [28] A. Ern, J.-L. Guermond, Weighting the edge stabilization, *SIAM J. Numer. Anal.* 51 (3) (2013) 1655–1677.
 - [29] E. F. Toro, *Riemann solvers and numerical methods for fluid dynamics*, 3rd Edition, Springer-Verlag, Berlin, 2009, a practical introduction. doi:10.1007/b79761.
URL <http://dx.doi.org/10.1007/b79761>
 - [30] J. L. Guermond, B. Popov, Invariant domains and first-order continuous finite element approximation for hyperbolic systems, *SIAM Journal on Numerical Analysis* 54 (4) (2016) 2466–2489. arXiv:<http://dx.doi.org/10.1137/16M1074291>, doi:10.1137/16M1074291.
URL <http://dx.doi.org/10.1137/16M1074291>
 - [31] C. A. J. Fletcher, *Computational techniques for fluid dynamics. 1*, Springer Series in Computational Physics, Springer-Verlag, Berlin, 1988, fundamental and general techniques.
 - [32] P. Wesseling, *Principles of computational fluid dynamics*, Vol. 29 of Springer Series in Computational Mathematics, Springer-Verlag, Berlin, 2001. doi:10.1007/978-3-642-05146-3.
URL <http://dx.doi.org/10.1007/978-3-642-05146-3>
 - [33] D. Kuzmin, M. Möller, Algebraic flux correction. II. Compressible Euler equations, in: *Flux-corrected transport*, Sci. Comput., Springer, Berlin, 2005, pp. 207–250. doi:10.1007/3-540-27206-2_7.
URL http://dx.doi.org/10.1007/3-540-27206-2_7
 - [34] J. Hoffman, J. Jansson, C. Degirmenci, N. Jansson, M. Nazarov, Unicorn: a unified continuum mechanics solver, *Automated solution of differential equations by the finite element method* (Eds. A. Logg, K.-A. Mardal, G.N. Wells), Springer, 2011.
 - [35] J. Hoffman, J. Jansson, R. Vilela de Abreu, N. C. Degirmenci, N. Jansson, K. Müller, M. Nazarov, J. H. Spühler, Unicorn: parallel adaptive finite element simulation of turbulent flow and fluid-structure interaction for deforming domains and complex geometry, *Comput. & Fluids* 80 (2013) 310–319. doi:10.1016/j.compfluid.2012.02.003.
URL <http://dx.doi.org/10.1016/j.compfluid.2012.02.003>
 - [36] R. A. DeVore, Nonlinear approximation, in: *Acta numerica*, 1998, Vol. 7 of Acta Numer., Cambridge Univ. Press, Cambridge, 1998, pp. 51–150. doi:10.1017/S0962492900002816.
URL <http://dx.doi.org/10.1017/S0962492900002816>
 - [37] R. Liska, B. Wendroff, Comparison of several difference schemes on 1D and 2D test problems for the Euler equations, *SIAM J. Sci. Comput.* 25 (3) (2003) 995–1017 (electronic). doi:10.1137/S1064827502402120.
URL <http://dx.doi.org/10.1137/S1064827502402120>
 - [38] A. F. Emery, An evaluation of several differencing methods for inviscid fluid flow problems, *J. Computational Phys.* 2 (1968) 306–331.
 - [39] P. Woodward, P. Colella, The numerical simulation of two-dimensional fluid flow with strong shocks, *J. Comput. Phys.* 54 (1) (1984) 115–173. doi:10.1016/0021-9991(84)90142-6.
URL [http://dx.doi.org/10.1016/0021-9991\(84\)90142-6](http://dx.doi.org/10.1016/0021-9991(84)90142-6)
 - [40] J. W. Banks, W. D. Henshaw, D. W. Schwendeman, A. K. Kapila, A study of detonation propagation and diffraction with compliant confinement, *Combust. Theory Model.* 12 (4) (2008) 769–808. doi:10.1080/13647830802123564.
URL <http://dx.doi.org/10.1080/13647830802123564>
 - [41] J. Niederhaus, D. Ranjan, J. Oakley, M. Anderson, J. Greenough, R. Bonazza, Computations in 3d for shock-induced distortion of a light spherical gas inhomogeneity, in: K. Hannemann, F. Seiler (Eds.), *Shock Waves*, Springer Berlin Heidelberg, 2009, pp. 1169–1174.
 - [42] J. O. Langseth, R. J. LeVeque, A wave propagation method for three-dimensional hyperbolic conservation laws, *J. Comput. Phys.* 165 (1) (2000) 126–166. doi:10.1006/jcph.2000.6606.
URL <http://dx.doi.org/10.1006/jcph.2000.6606>
 - [43] C. W. Schulz-Rinne, Classification of the Riemann problem for two-dimensional gas dynamics, *SIAM J. Math. Anal.* 24 (1) (1993) 76–88. doi:10.1137/0524006.
URL <http://dx.doi.org/10.1137/0524006>
 - [44] H. J. Schroll, F. Svensson, A bi-hyperbolic finite volume method on quadrilateral meshes, *J. Sci. Comput.* 26 (2) (2006) 237–260. doi:10.1007/s10915-004-4927-9.
URL <http://dx.doi.org/10.1007/s10915-004-4927-9>
 - [45] H. Holden, K.-A. Lie, N. H. Risebro, An unconditionally stable method for the Euler equations, *J. Comput. Phys.* 150 (1) (1999) 76–96. doi:10.1006/jcph.1998.6164.
URL <http://dx.doi.org/10.1006/jcph.1998.6164>
 - [46] J. P. Boris, D. L. Book, Flux-corrected transport. I. SHASTA, a fluid transport algorithm that works [*J. Comput. Phys.* 11 (1973), no. 1, 38–69], *J. Comput. Phys.* 135 (2) (1997) 170–186, with an introduction by Steven T. Zalesak, Commemoration of the 30th anniversary of *J. Comput. Phys.*
 - [47] S. T. Zalesak, Fully multidimensional flux-corrected transport algorithms for fluids, *J. Comput. Phys.* 31 (3) (1979) 335–362.
 - [48] J.-L. Guermond, M. Nazarov, B. Popov, Y. Yang, A second-order maximum principle preserving Lagrange finite element technique for nonlinear scalar conservation equations, *SIAM J. Numer. Anal.* 52 (4) (2014) 2163–2182. doi:10.1137/130950240.
URL <http://dx.doi.org/10.1137/130950240>

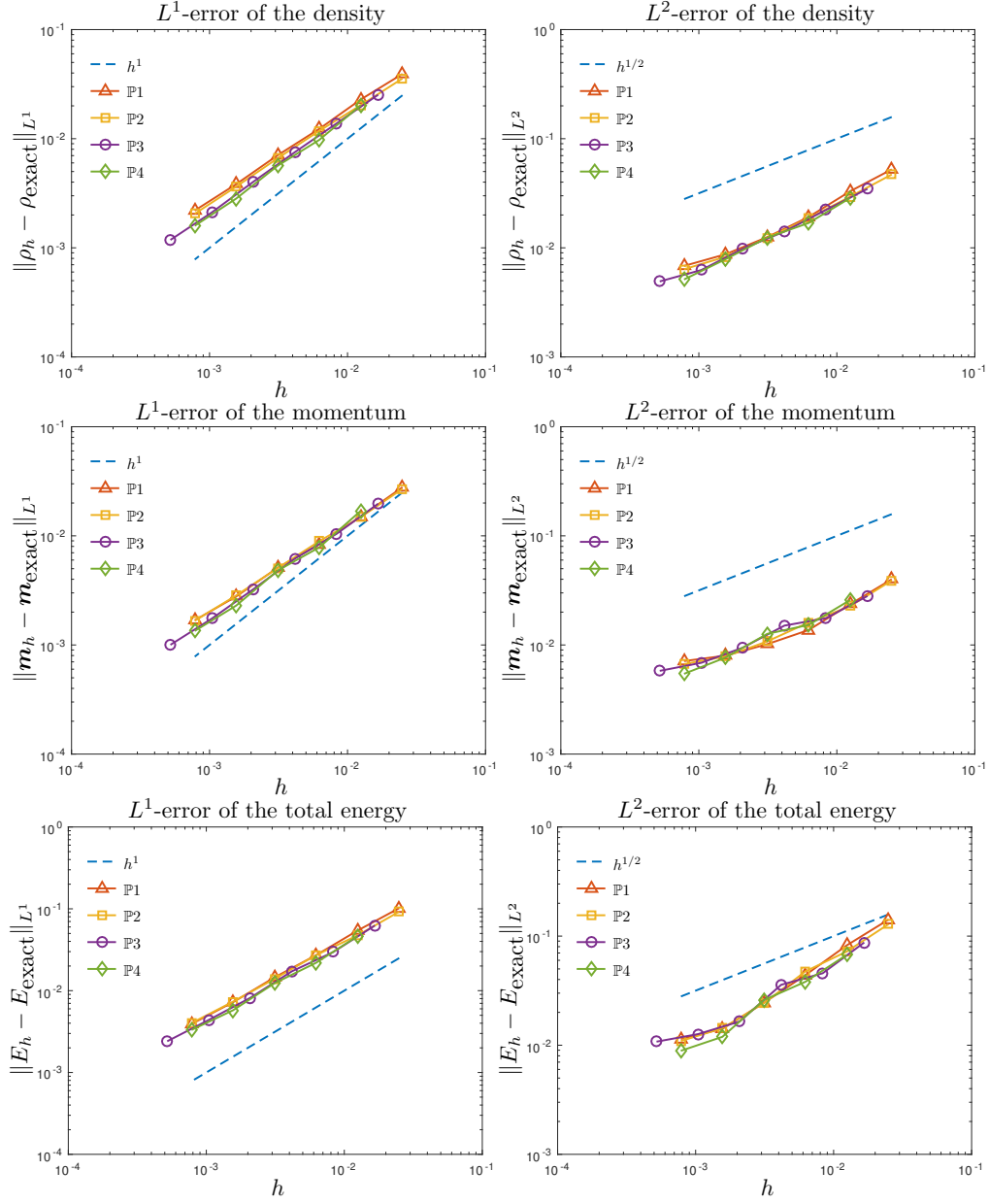


Figure 6: Sod shock-tube problem: convergence history for conservative variables (ρ, \mathbf{m}, E), upper and lower left panels, and the scaled magnitude of P_1 entropy viscosity, lower right panel.

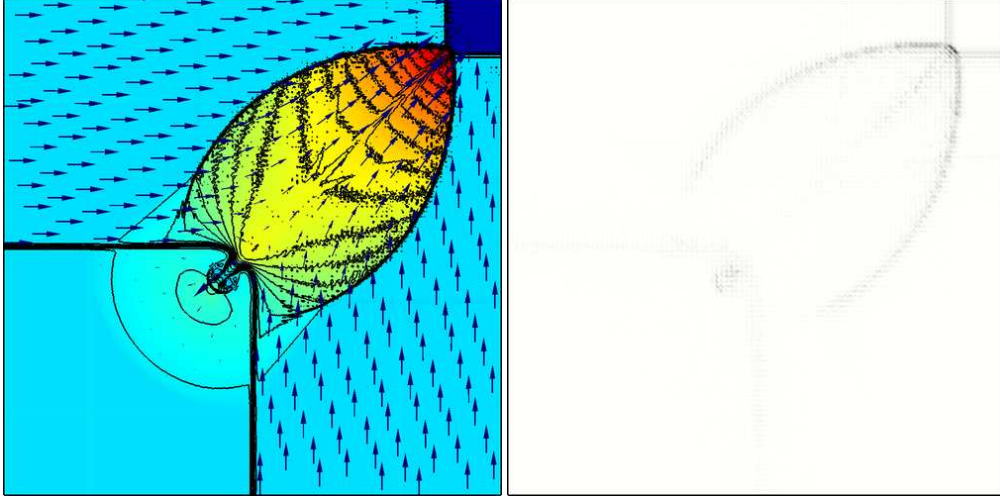


Figure 7: 2D Riemann problem: in the left panel 30 contours lines of density from 0.54 to 1.7, pressure in color $p \in [0.38, 2.24]$, and velocity by arrows are plotted; in the right panel the entropy viscosity $\mu = [0, 1.4\text{E-}04]$ is displayed. The computation is done on the unit square of 100×100 mesh points using \mathbb{P}_4 approximation until $t = 0.25$.

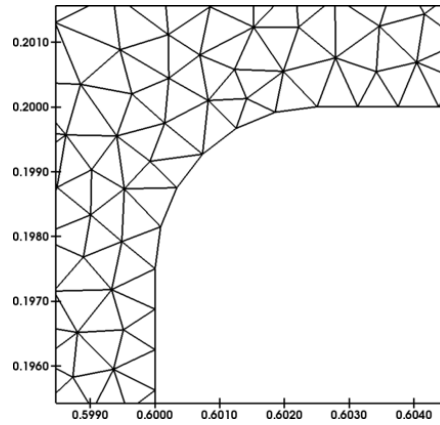


Figure 8: Step: Zoom close to the singularity point

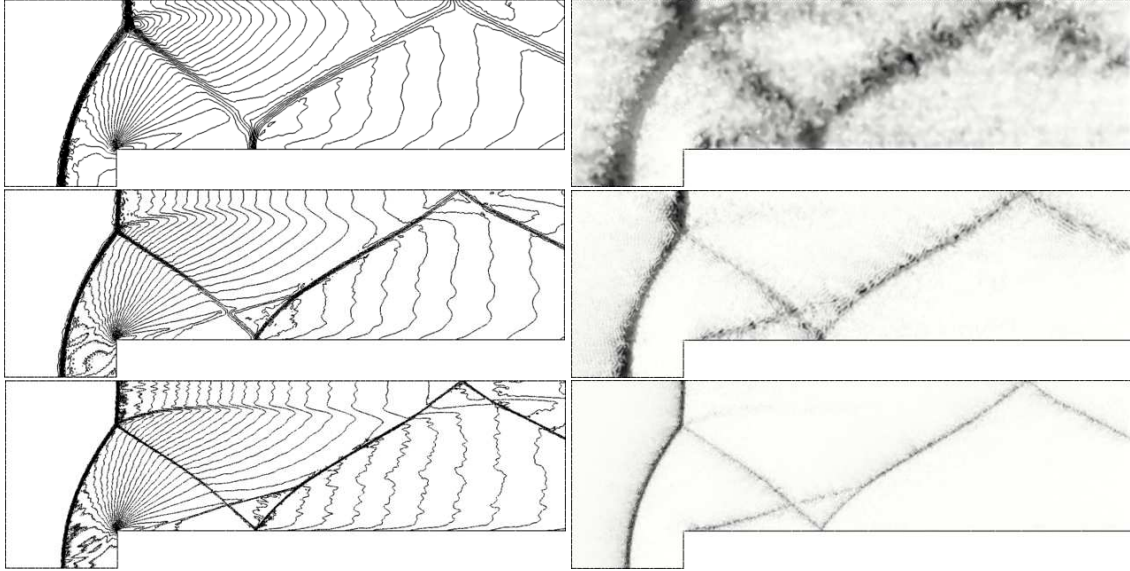


Figure 9: Step: 30 contour lines of density at the left panel and the magnitude of the entropy viscosity is at the right panel. The first row: \mathbb{P}_1 approximation, $h_K \approx 0.025$, $\mu = [3.9\text{E-}06, 2.6\text{E-}02]$; The second row: \mathbb{P}_2 approximation, $h_K \approx 0.025$, $\mu = [3.1\text{E-}07, 1.5\text{E-}02]$; The third row: \mathbb{P}_2 approximation, $h_K \approx 0.0125$, $\mu = [3.2\text{E-}07, 6.9\text{E-}03]$. The plots correspond to the solution at the final time $t = 4$.

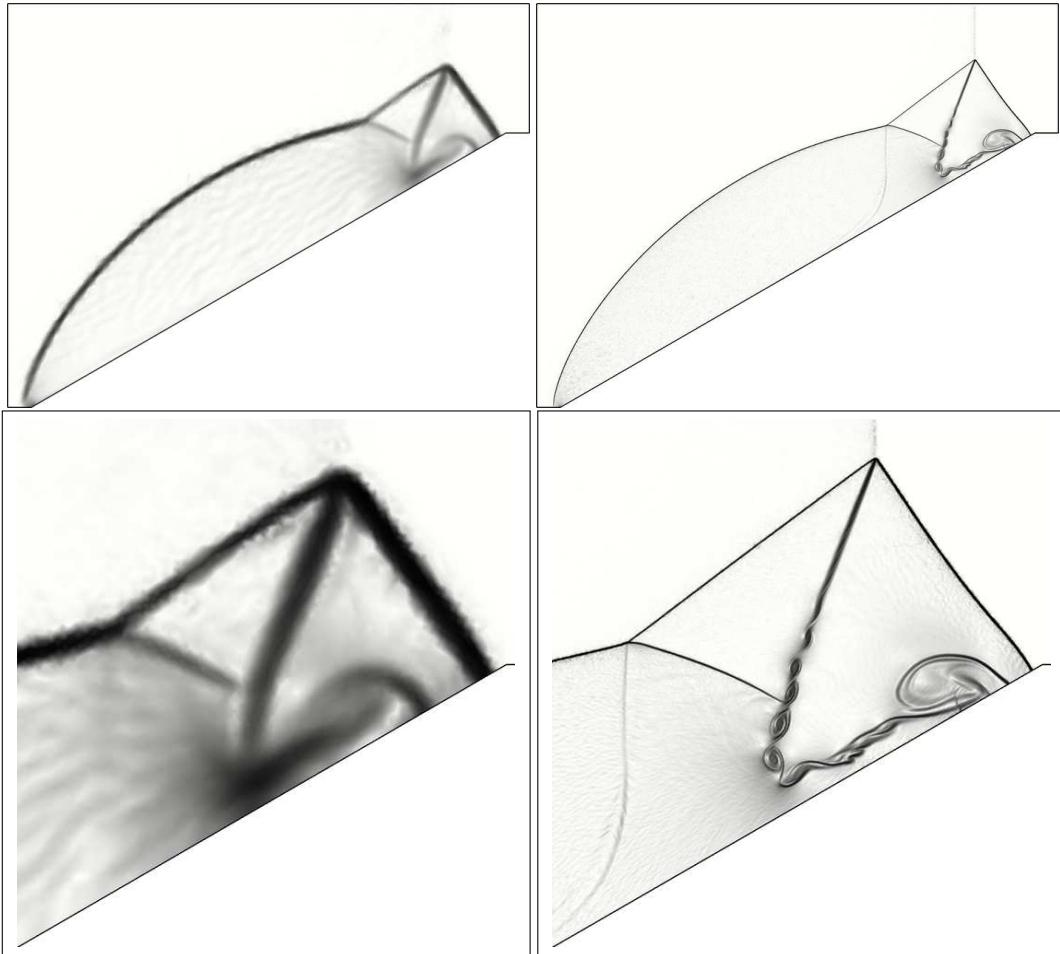


Figure 10: Double Mach reflection: Schlieren diagram of the vertical momentum m_2 at $t = 0.2$. The left panel describes \mathbb{P}_2 approximation in a coarse mesh with $h_K \approx 0.025$, the right panel plots \mathbb{P}_2 approximation in a fine mesh with $h_K \approx 0.0025$.

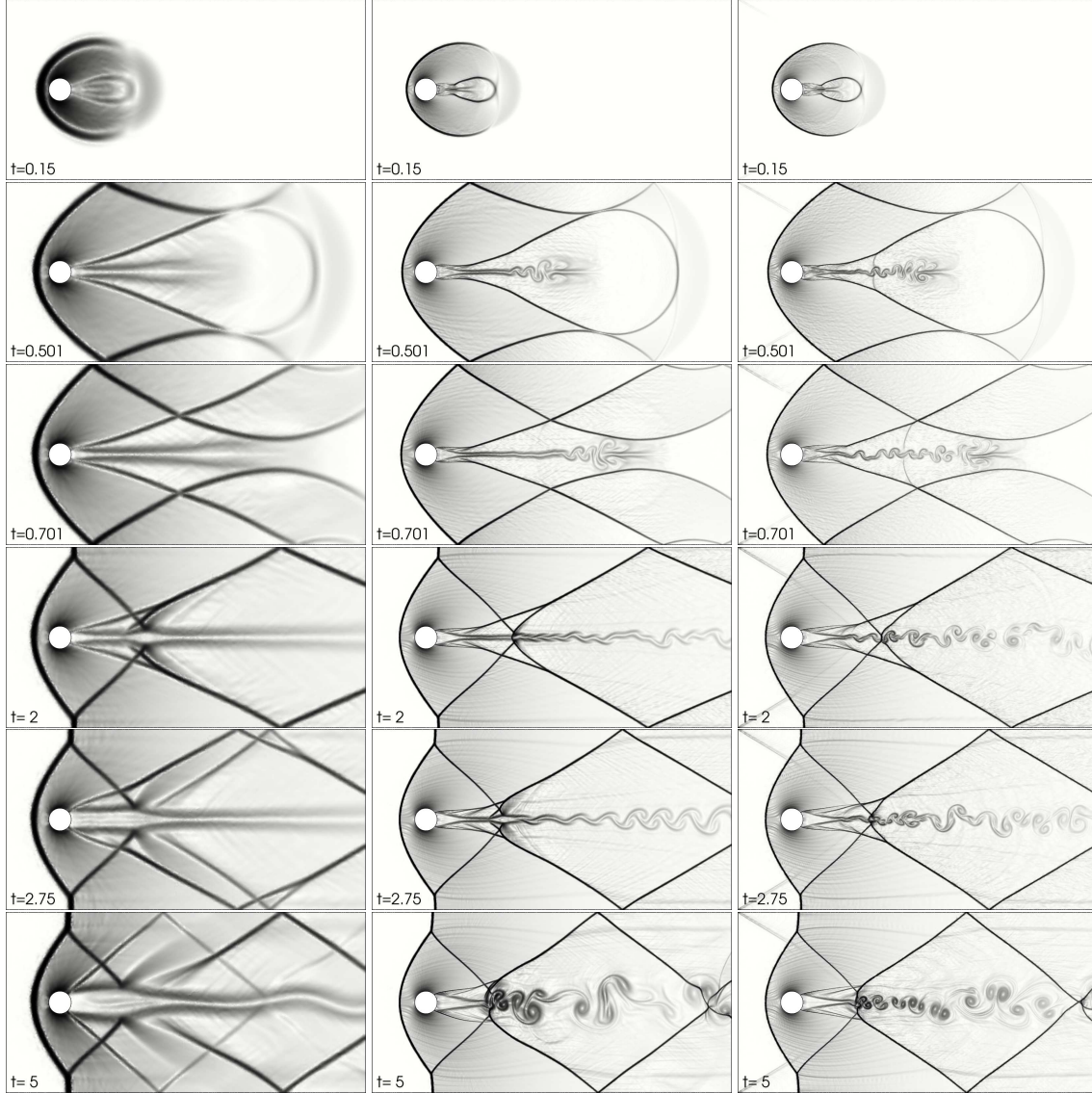


Figure 11: Supersonic Mach 2 flow around circular cylinder: Schlieren diagram of density. The left pannel plots \mathbb{P}_1 solution on a coarse mesh of $h_K \approx 0.01$ with 26,626 points and 52,612 cells, the middle panel plots \mathbb{P}_1 solution on a fine mesh of $h_K \approx 0.003$ with 256,216 points and 508,272 cells, the right pannel plots \mathbb{P}_2 approximation on a fine mesh of $h_K \approx 0.006$ with 64,020 points 127,068 cells

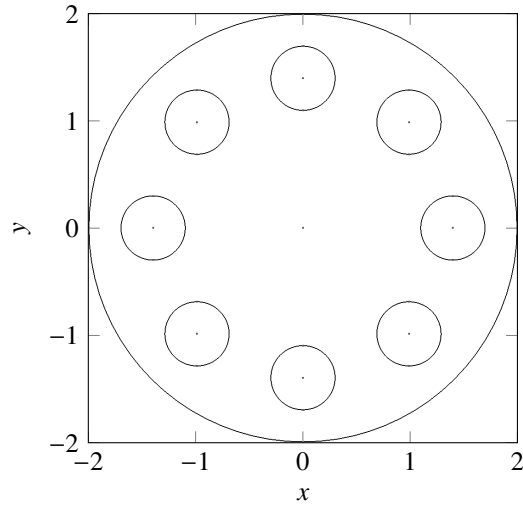


Figure 12: The geometry of the explosion test

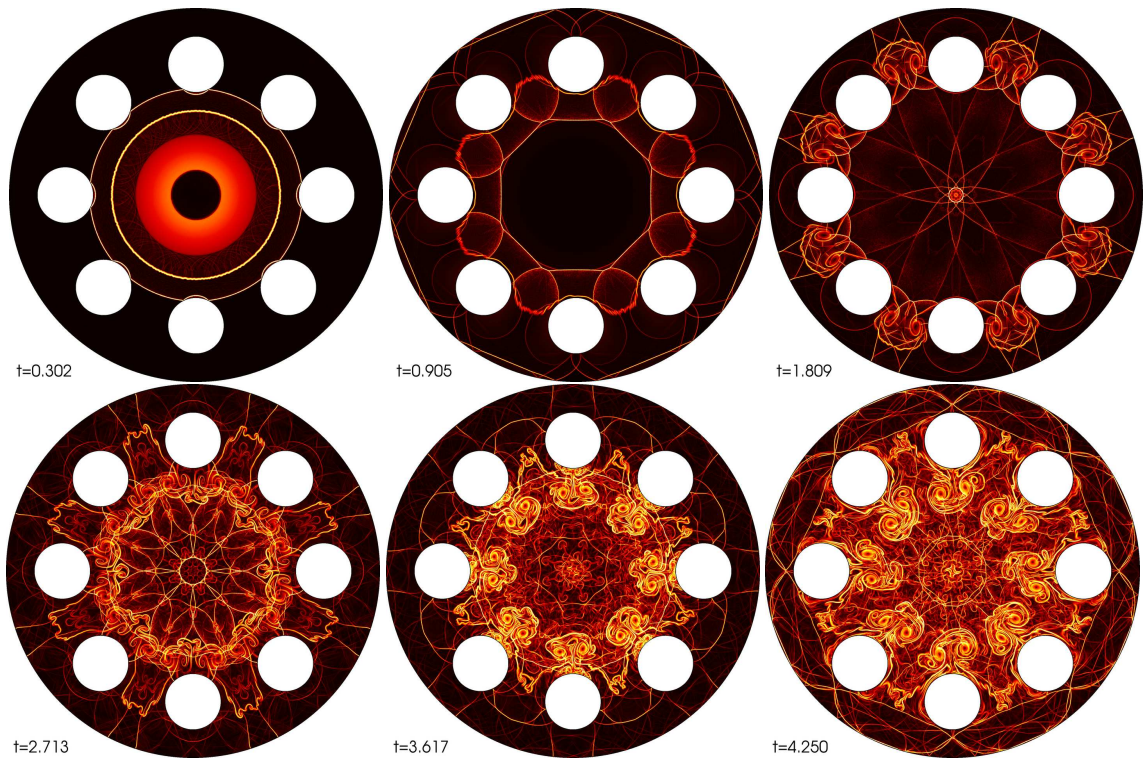


Figure 13: 2D Explosion problem: Schlieren diagram of the density. The solution is presented in different time levels using 1,539,650 \mathbb{P}_2 nodes.

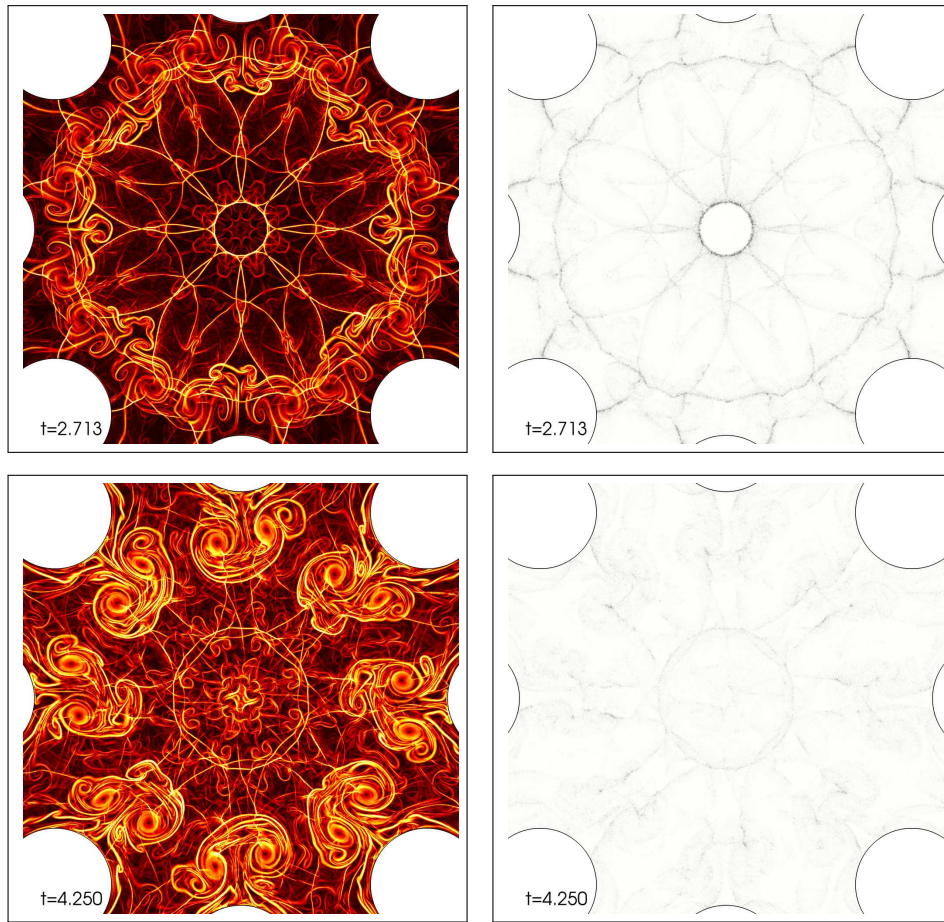


Figure 14: 2D Explosion problem: Schlieren diagram of the density on the left panel and the magnitude of the entropy viscosity μ_h on the right panel. The magnitude of the entropy viscosity changes between $1\text{E-}10$ to $1\text{E-}3$. Zoom of the small scales vortices, shocks and contact discontinuities close to the origin.

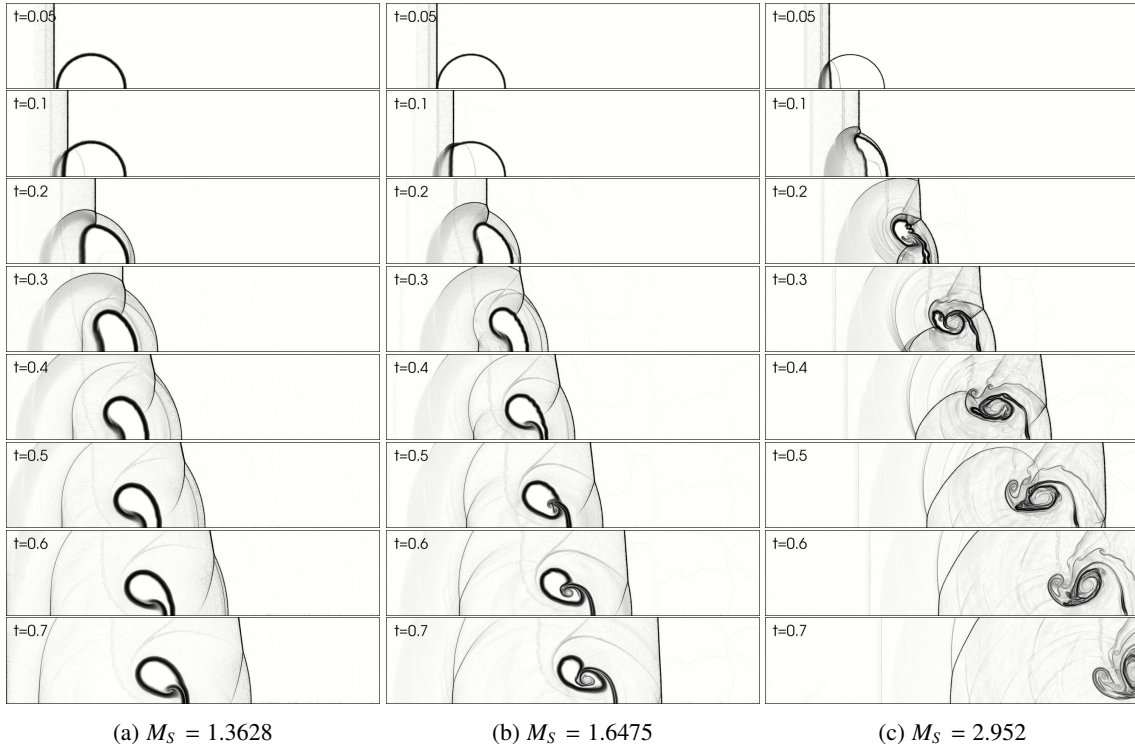


Figure 15: Shock-bubble interaction: Schlieren diagram of density. Time evolution solution of \mathbb{P}_2 finite element approximation in the mesh of mesh-size $h_K \approx 0.0035$. The columns correspond to behind shock pressures 2, 3 and 10 respectively.

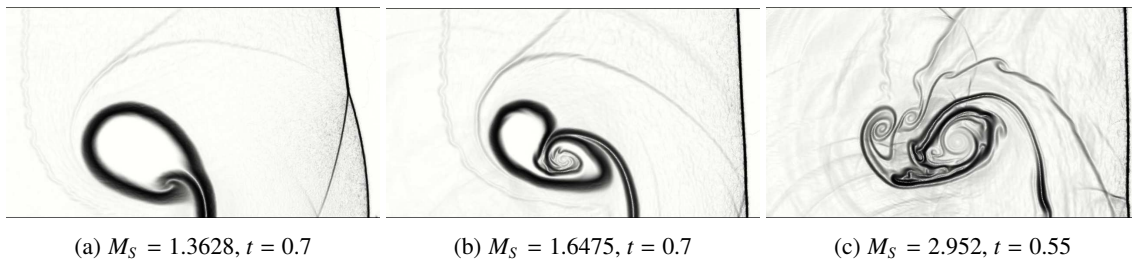


Figure 16: Shock-bubble interaction: Schlieren diagram of density. The tip of the bubble is plotted for later time for all Mach numbers.